



Escaping Helium and a Highly Muted Spectrum Suggest a Metal-enriched Atmosphere on Sub-Neptune GJ 3090 b from JWST Transit Spectroscopy

Eva-Maria Ahrer¹ , Michael Radica^{2,3,20} , Caroline Piaulet-Ghorayeb^{2,3,21} , Eshan Raul⁴ , Lindsey Wiser⁵ , Luis Welbanks⁵ , Lorena Acuña⁶ , Romain Allart³ , Louis-Philippe Coulombe³ , Amy Louca^{7,8} , Ryan MacDonald⁹ , Morgan Saidel¹⁰ , Thomas M. Evans-Soma^{1,11} , Björn Benneke³ , Duncan Christie¹ , Thomas G. Beatty⁴ , Charles Cadieux³ , Ryan Cloutier¹² , René Doyon³ , Jonathan J. Fortney¹³ , Anna Gagnebin¹³ , Cyril Gapp^{1,14} , Hamish Innes^{15,16} , Heather A. Knutson¹⁰ , Thaddeus Komacek¹⁷ , Joshua Krissansen-Totton¹⁸ , Yamila Miguel^{7,8} , Raymond Pierrehumbert¹⁷ , Pierre-Alexis Roy³ , and Hilke E. Schlichting¹⁹

¹Max-Planck-Institut für Astronomie, Königstuhl 17, 69117 Heidelberg, Germany; ahrer@mpia.de

²Department of Astronomy & Astrophysics, University of Chicago, 5640 South Ellis Avenue, Chicago, IL 60637, USA

³Department of Physics and Trotter Institute for Research on Exoplanets, Université de Montréal, Montréal, QC, Canada

⁴Department of Astronomy, University of Wisconsin–Madison, Madison, WI 53706, USA

⁵School of Earth & Space Exploration, Arizona State University, Tempe, AZ 85287, USA

⁶Max Planck Institute for Astronomy, Königstuhl 17, D-69117 Heidelberg, Germany

⁷SRON Netherlands Institute for Space Research, Niels Bohrweg 4, 2333 CA Leiden, The Netherlands

⁸Leiden Observatory, Leiden University, P.O. Box 9513, 2300 RA Leiden, The Netherlands

⁹Department of Astronomy, University of Michigan, Ann Arbor, MI, USA

¹⁰Division of Geological and Planetary Sciences, California Institute of Technology, Pasadena, CA 91125, USA

¹¹School of Information and Physical Sciences, University of Newcastle, Callaghan, NSW, Australia

¹²Department of Physics & Astronomy, McMaster University, 1280 Main Street West, Hamilton, ON, L8S 4L8, Canada

¹³Department of Astronomy & Astrophysics, University of California, Santa Cruz, CA 95064, USA

¹⁴Department of Physics and Astronomy, Heidelberg University, Im Neuenheimer Feld 226, D-69120 Heidelberg, Germany

¹⁵Department of Earth Sciences, Freie Universität Berlin, Malteserstr. 74-100, 12249 Berlin, Germany

¹⁶Institute of Planetary Research, German Aerospace Center (DLR), Rutherfordstraße 2, 12489 Berlin, Germany

¹⁷Department of Physics, University of Oxford, Oxford, OX1 3PW, UK

¹⁸Department of Earth and Space Sciences/Astrobiology Program, University of Washington, Seattle, WA, USA

¹⁹Department of Earth, Planetary, and Space Sciences, University of California, Los Angeles, CA 90095, USA

Received 2024 December 16; revised 2025 April 9; accepted 2025 April 14; published 2025 May 15

Abstract

Sub-Neptunes, the most common planet type, remain poorly understood. Their atmospheres are expected to be diverse, but their compositions are challenging to determine, even with JWST. Here, we present the first JWST spectroscopic study of the warm sub-Neptune GJ 3090 b ($2.13 R_{\oplus}$, $T_{\text{eq,A}} = 0.3 \sim 700$ K), which orbits an M2V star, making it a favorable target for atmosphere characterization. We observed four transits of GJ 3090 b: two each using JWST NIRISS/SOSS and NIRSpec/G395H, yielding wavelength coverage from 0.6 to $5.2 \mu\text{m}$. We detect the signature of the 10833 \AA metastable helium triplet at a statistical significance of 5.5σ with an amplitude of 434 ± 79 ppm, marking the first such detection in a sub-Neptune with JWST. This amplitude is significantly smaller than predicted by solar-metallicity forward models, suggesting a metal-enriched atmosphere that decreases the mass-loss rate and attenuates the helium feature amplitude. Moreover, we find that stellar contamination, in the form of the transit light source effect, dominates the NIRISS transmission spectra, with unocculted spot and faculae properties varying across the two visits separated in time by approximately 6 months. Free retrieval analyses on the NIRSpec/G395H spectrum find tentative evidence for highly muted features and a lack of CH_4 . These findings are best explained by a high-metallicity atmosphere ($>100\times$ solar at 3σ confidence for clouds at $\sim\mu\text{bar}$ pressures) using chemically consistent retrievals and self-consistent model grids. Further observations of GJ 3090 b are needed for tighter constraints on the atmospheric abundances and to gain a deeper understanding of the processes that led to its potential metal enrichment.

Unified Astronomy Thesaurus concepts: Exoplanet atmospheres (487); Exoplanet atmospheric composition (2021); Transmission spectroscopy (2133); Exoplanets (498); James Webb Space Telescope (2291)

1. Introduction

In the decades since the first exoplanets were found around Sun-like stars (e.g., M. Mayor & D. Queloz 1995;

D. Charbonneau et al. 2000; G. W. Henry et al. 2000), thousands of new planets have been detected. One of the most impactful outcomes of these discoveries is that planets intermediate in mass and radius to Earth and Neptune, so-called “sub-Neptunes,” are, in fact, the most common type of planet in the galaxy (W. J. Borucki et al. 2010; B. J. Fulton et al. 2017; B. J. Fulton & E. A. Petigura 2018). Moreover, population-level studies have found that the radius distribution of these small planets shows a gap in occurrence rate between 1.8 and $2.0 R_{\oplus}$ around FGK stars known as the “radius valley” (B. J. Fulton et al. 2017; E. A. Petigura et al. 2022). This is

²⁰ NSERC Postdoctoral Fellow.

²¹ E. Margaret Burbridge Postdoctoral Fellow.



commonly thought to divide these exoplanets into a smaller, likely rocky population and a larger, gaseous population (e.g., E. J. Lee & E. Chiang 2016; J. E. Owen & Y. Wu 2017; S. Ginzburg et al. 2018). However, the picture is blurrier for sub-Neptunes around M dwarf stars, which show a less well-defined radius valley (R. Cloutier & K. Menou 2020; C. S. K. Ho et al. 2024; J. Venturini et al. 2024), and a significant population that has densities suggestive of a substantial volatile content (R. Luque & E. Pallé 2022; J. G. Rogers et al. 2023).

Previous modeling efforts have illustrated the impacts of atmospheric evolution processes (e.g., core-powered mass loss, S. Ginzburg et al. 2016, 2018; A. Gupta & H. E. Schlichting 2019; and photoevaporation; E. D. Lopez et al. 2012; J. E. Owen & Y. Wu 2017; J. G. Rogers et al. 2021) on the present-day composition and structure of sub-Neptunes. Such mass-loss processes in particular are well traced (if not necessarily well constrained; e.g., M. Zhang et al. 2025) by observations of the metastable 10833 Å He triplet (A. Oklopčić & C. M. Hirata 2018; A. Oklopčić 2019). To date, numerous detections of escaping atmospheres have been made (e.g., M. Mansfield et al. 2018; L. Nortmann et al. 2018; J. J. Spake et al. 2018, 2021; R. Allart et al. 2019; J. Kirk et al. 2020; M. Zhang et al. 2022a, 2025; G. Guilluy et al. 2024; J. Orell-Miquel et al. 2024; S. Vissapragada et al. 2024a), with He observations of young mini-Neptunes in particular highlighting the impacts of mass loss in sculpting the radius valley around Sun-like stars (M. Zhang et al. 2022a, 2022b, 2023). Recently, JWST observations, particularly with NIRISS/SOSS (e.g., G. Fu et al. 2023; M. Fournier-Tondreau et al. 2024), have proved efficient at detecting escaping He from exoplanet atmospheres, potentially providing a new avenue to examine the effects of atmosphere loss on the population of sub-Neptunes orbiting late-type stars.

In addition to atmosphere loss, a range of possible formation and migration histories (e.g., R. Burn et al. 2024), as well as interactions with the surface (e.g., with a magma ocean; Y. Chachan & D. J. Stevenson 2018; E. S. Kite et al. 2019; T. Lichtenberg et al. 2021; H. E. Schlichting & E. D. Young 2022), can also result in a wide range of bulk compositions for sub-Neptunes. Critically, though, it has long been known that the nature of sub-Neptune exoplanets cannot be uniquely revealed by bulk density measurements alone (L. A. Rogers & S. Seager 2010; D. Valencia 2010), with atmosphere observations being the necessary piece of information to unveil the nature of this most common class of planets in the galaxy.

Prior to the JWST era, observational studies of sub-Neptune atmospheres (aside from helium escape) were routinely hindered by insufficient wavelength coverage and sensitivity, resulting in degeneracies in atmosphere composition due to clouds (e.g., Z. K. Berta et al. 2012; J. L. Bean et al. 2013; L. Kreidberg et al. 2014; B. Benneke et al. 2019a; P.-A. Roy et al. 2023), overlap in molecular absorption (e.g., B. Benneke et al. 2019b; A. Tsiaras et al. 2019; B. Bézard et al. 2022), or stellar contamination (e.g., T. Barclay et al. 2021; B. Edwards et al. 2021; T. Mikal-Evans et al. 2023).

However, with the launch of JWST, we have now begun to uniquely constrain the chemical composition and thereby uncover the surprising diversity of sub-Neptune atmospheres. N. Madhusudhan et al. (2023) reported carbon-bearing molecules in the atmosphere of the cool, 255 K sub-Neptune K2-18 b from a JWST NIRISS and NIRSpec transmission

spectrum and suggested that the inferred composition was consistent with predictions for temperate ocean-covered planets with H₂-rich atmospheres (i.e., Hycean planets; e.g., N. Madhusudhan et al. 2021). Planetary conditions that are consistent with predictions for Hycean environments were also reported by M. Holmberg & N. Madhusudhan (2024) for the 354 K sub-Neptune TOI-270 d (which was also previously studied by the Hubble Space Telescope, HST; T. Mikal-Evans et al. 2023) using NIRSpec observations. When combining the NIRSpec observations analyzed by M. Holmberg & N. Madhusudhan (2024) with additional NIRISS data, B. Benneke et al. (2024) find a similar chemical composition (i.e., H₂O and CO₂ abundances) for the atmosphere of TOI-270 d to that reported by M. Holmberg & N. Madhusudhan (2024) but interpret the chemical conditions as signatures of a volatile-rich, miscible-envelope scenario, where roughly half the mass of TOI-270 d’s envelope is composed of high-mean-molecular-weight (MMW) volatiles well mixed with H₂/He. The interpretation of the inferred chemical composition for sub-Neptunes and their implications for the diversity in their climate and habitable conditions is a highly active and growing area of research (e.g., H. Innes et al. 2023; G. J. Cooke & N. Madhusudhan 2024; C. R. Glein 2024; J. Leconte et al. 2024; F. E. Rigby et al. 2024; O. Shorttle et al. 2024; N. F. Wogan et al. 2024; S. P. Schmidt et al. 2025).

More recently, C. Piaulet-Ghorayeb et al. (2024) revealed a H₂O-rich “steam atmosphere” on the warm, 616 K sub-Neptune GJ 9827 d, and evidence for S-bearing compounds has been found in the atmospheres of GJ 3470 b by T. G. Beatty et al. (2024) and L 98-59 d by A. Banerjee et al. (2024) and A. Gressier et al. (2024). While the previous five planets have suggested metallicities in the range of $\sim 100\text{--}500\times$ solar, a much larger, $1000\times$ solar metallicity was found for the canonical sub-Neptune GJ 1214 b (E. Schlawin et al. 2024) along with significant amounts of haze (P. Gao et al. 2023; K23; K. Ohno et al. 2025; E. Schlawin et al. 2024).

These early results demonstrate that the diversity of sub-Neptunes extends well beyond typical ideas of rocky “super-Earths” and H₂/He-rich “mini-Neptunes.” They have also shown that robustly constraining atmospheric metallicity is a challenging feat due to the increasing variety of unknowns when it comes to sub-Neptune atmospheres. To further develop our understanding of sub-Neptunes as a population, we require a larger sample size of planets with well-characterized atmospheres.

1.1. The GJ 3090 System

GJ 3090 is an M2V star hosting one confirmed planet: the sub-Neptune GJ 3090 b (J. M. Almenara et al. 2022). The star was determined to have a mass of $0.519 \pm 0.013 M_{\odot}$ and a radius of $0.516 \pm 0.016 R_{\odot}$ (see Table 1). It is a relatively bright and nearby star with $J_{\text{mag}} = 8.168 \pm 0.021$ (Two Micron All Sky Survey; M. F. Skrutskie et al. 2006) and a distance of 22.444 ± 0.013 pc (J. M. Almenara et al. 2022).

Using observations with the Transiting Exoplanet Survey Satellite (TESS; G. R. Ricker et al. 2015), J. M. Almenara et al. (2022) identified GJ 3090 b with a radius of $2.13 \pm 0.11 R_{\oplus}$ and a period of 2.8531054 ± 0.0000023 days. In addition, the High Accuracy Radial Velocity Planet Searcher (HARPS) spectrograph (M. Mayor et al. 2003) was used to determine the planet’s mass as $3.34 \pm 0.72 M_{\oplus}$, resulting in a mean density of $1.89^{+0.52}_{-0.45} \text{ g cm}^{-3}$ (J. M. Almenara et al. 2022). The equilibrium

Table 1
Stellar Parameters of GJ 3090

Parameter	Value
Effective temperature, T_{eff} (K)	3556 ± 70
Spectral type	M2V
Metallicity, Z ([Fe/H])	-0.060 ± 0.120
Surface gravity, $\log(g)$ ($\log_{10}(\text{cm s}^{-2})$)	4.727 ± 0.029
Radius, R_s (R_{\odot})	0.516 ± 0.016
Mass, M_s (M_{\odot})	0.519 ± 0.013
Rotation period, P_{rot} (days)	17.65 ± 0.48

Note. As determined by J. M. Almenara et al. (2022) and adopted throughout this work.

temperature was determined to be $T_{\text{eq,A}=0.3} = 693 \pm 18$ K. The authors also found some evidence for an eccentric orbit, with a 95% confidence upper limit of $e < 0.32$. In addition to planet b, their radial velocity (RV) data suggest an outer planet candidate at a period of 13 days and a minimum mass of $17.1^{+8.9}_{-3.2} M_{\oplus}$, whose transits were not detected with TESS. We show GJ 3090 b in context with the population of sub-Neptunes in Figure 1. In particular, GJ 3090 b is the warmest of all sub-Neptunes with published atmosphere spectra, ~ 100 K warmer than GJ 9827 d and nearly double the temperature of K2-18 b. Recently, L. T. Parker et al. (2025) found no atmospheric signatures in GJ 3090 b’s atmosphere using four CRRES+ transits in the K band (sensitive to CH_4 , H_2O , NH_3 , and H_2S). Their study suggests a metal-rich atmosphere with $>150\times$ solar metallicity at an MMW of $>7.1 \text{ g mol}^{-1}$ and an unconstrained cloud layer.

J. M. Almenara et al. (2022) also showed that GJ 3090 exhibits photometric variations in the TESS light curves at a $\sim 1.5\%$ level with a period of 17.65 ± 0.48 days, which is consistent with the stellar rotation period inferred from the RV (~ 17.73 days) and archival WASP data (18.20 ± 0.40 days). Using the star’s rotation period and mass, J. M. Almenara et al. (2022) estimated the system to be relatively young ($1.02^{+0.15}_{-0.23}$ Gyr). Their analysis of common activity indicators in the HARPS spectra confirms that GJ 3090 is moderately active.

1.2. Structure of This Work

In this work, we add to the growing sample of sub-Neptunes with precise atmosphere observations by presenting the first JWST transmission spectrum of GJ 3090 b, a sub-Neptune at the outer edge of the radius valley. We outline our reduction and analysis of two transits with NIRISS/SOSS and two transits with NIRSpec/G395H in Sections 2 and 3, with special emphasis on metastable helium in Section 4. We present our atmosphere modeling in Section 5 and discuss our results in Section 6 before concluding in Section 7.

2. Observations and Data Analysis

The observations presented here were taken as part of JWST program GO 4098 (PIs: Benneke & Evans-Soma), with the purpose of “exploring the existence and diversity of volatile-rich water worlds.” Four transits of GJ 3090 b were observed with JWST, two with the NIRISS instrument (R. Doyon et al. 2023) in SOSS mode (L. Albert et al. 2023) on 2023 December 6 and 2024 July 4 covering the $0.6\text{--}2.8 \mu\text{m}$ wave band, and two with the NIRSpec instrument (S. M. Birkmann et al. 2022)

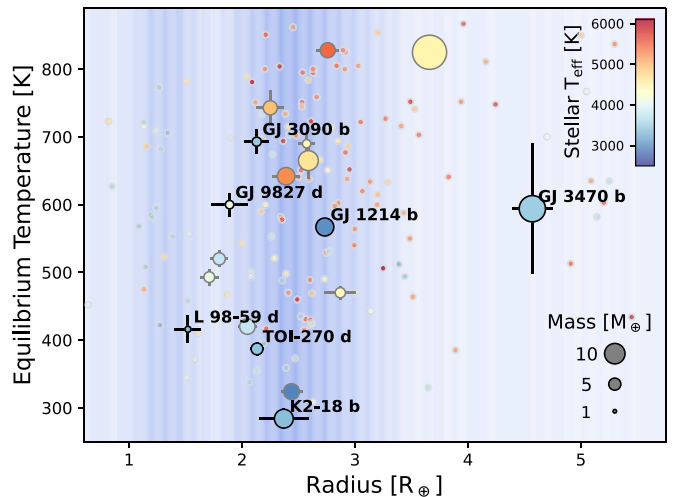


Figure 1. GJ 3090 b in context with the population of sub-Neptune planets in equilibrium temperature vs. planet radius space. Markers are colored by the effective temperature of the stellar host, and marker sizes reflect the planet mass. The background shading represents the distribution of sub-Neptune planets from B. J. Fulton et al. (2017), highlighting the radius valley near $1.7 R_{\oplus}$. Planets with published JWST near-infrared atmosphere spectra are outlined in black and labeled. Planets that will have JWST atmosphere observations by the end of Cycle 3 are outlined in gray.

using the G395H grating on 2023 August 2 and 2023 September 23, adding the $2.7\text{--}5.2 \mu\text{m}$ wavelength range.

2.1. NIRISS/SOSS

For the NIRISS/SOSS observations, we used two groups per integration and a total of 779 integrations, resulting in an overall observing time of 3.6 hr, which includes an out-of-transit time of ~ 2.3 hr and 1.281 hr of transit time (including ingress and egress). The readout mode was NISRAPID, and the subarray was SUBSTRIP256, providing the full $0.6\text{--}2.85 \mu\text{m}$ wavelength coverage (L. Albert et al. 2023).

2.1.1. *exo*TEDRF Reduction

We reduce the NIRISS/SOSS observations using *exo*-TEDRF (A. D. Feinstein et al. 2023; M. Radica et al. 2023; M. Radica 2024a), closely following the procedure laid out in B. Benneke et al. (2024) and M. Radica et al. (2024). We follow the standard *Stage1* and *Stage2* steps, as has been done in many other works (e.g., O. Lim et al. 2023; M. Radica et al. 2023, 2025; C. Cadieux et al. 2024; M. Fournier-Tondreau et al. 2024; C. Piaulet-Ghorayeb et al. 2024) and note any specific alterations here. In particular, due to the low number of groups observed up the ramp, we use the time-domain cosmic-ray detection algorithm outlined in M. Radica et al. (2024), with an outlier threshold of 5σ . Furthermore, we perform a piecewise background subtraction, finding optimal pre- and poststep scaling values of 0.62686 and 0.64511 compared to the reference background model, and we perform the $1/f$ noise correction at the integration level using the *scale-achromatic-window* method identically to B. Benneke et al. (2024).

We extract the stellar spectra using a simple box aperture with a width of 30 pixels, which we find minimizes the out-of-transit baseline scatter in the white light curve. Any dilution resulting from the order 1 and order 2 self-contamination is expected to be negligible (A. Darveau-Bernier et al. 2022;

M. Radica et al. 2022), and indeed, we find no difference in the resulting transmission spectra when applying the ATOCA extraction algorithm, which explicitly models the order overlap. Due to the judicious choice of telescope aperture position angle for these observations, there are no background contaminants, either dispersed or undispersed, affecting these spectra.

2.1.2. NAMELESS Reduction

The NAMELESS reduction pipeline (L.-P. Coulombe et al. 2023, 2025) starts with the uncalibrated files and allows us to run `rwst`'s Stages 1 and 2 (H. Bushouse et al. 2023) with modifications and perform other calibrations in between the default steps. We apply the following default steps: superbias subtraction, reference pixel correction, nonlinearity correction, ramp fitting, and flat-fielding. We continue with a manual bad-pixel correction, masking the ones that are consistently different from the surrounding values (e.g., by being negative or abnormally high). We correct the value of these bad pixels at all integrations using the `scipy.interpolate.griddata` bicubic interpolation function.

This is followed by a background subtraction where the background model provided by STScI²² is scaled to match the observed background. For that, we also use two independent scaling values, accounting for the characteristic abrupt transition in the intensity of the background flux.

Because the integrations consist of only two groups for this data set, the jump detection step is automatically skipped by the `rwst` pipeline. We thus correct for cosmic rays using the same method as described in L.-P. Coulombe et al. (2025), in which we compute the running median of all pixels, considering a window of 11 integrations, and clip all counts that deviate by more than 4σ from its median.

The $1/f$ noise is corrected by using a column-by-column scaling as described in L.-P. Coulombe et al. (2023, 2025). Given that the $1/f$ noise can vary over the length of a single column, we compute this scaling factor separately for order 1 and order 2 considering only pixels that are within a 30 pixel window from the center of the traces. When computing the scaling values for order 2, we do not consider pixels that overlap with the window of order 1. The $1/f$ values computed from order 1 are subtracted from the full columns, whereas those computed from order 2 are subtracted only from its window.

We extract the NIRISS/SOSS spectroscopic light curves from the first and second order using a simple box aperture with a width of 36 pixels.

2.2. NIRSpec/G395H

For each observation of GJ 3090 b with NIRSpec/G395H, four groups and 2845 integrations were used, summing to an overall exposure time of 3.6 hr, which consists of ~ 2.3 hr of out-of-transit time and 1.28 hr of transit time (including ingress and egress). NRSRAPID was the readout mode used for taking these NIRSpec observations in combination with the SUB2048 subarray.

2.2.1. ExoTDRF Reduction

We also reduce both NIRSpec/G395H visits with `ExoTDRF`, which has been recently upgraded to also handle NIRSpec data (M. Radica 2024a), applying many of the same routines originally developed for SOSS observations. For both visits, we apply the standard `Stage1` steps as for the SOSS observations, skipping the reference pixel correction, which we find imparts row-correlated noise, particularly to the NRS2 detector. We perform a $1/f$ noise correction (which also serves to subtract background emission) at the group level by subtracting the median value of each column, masking all bad pixels as well as pixels within 8 pixels above or below the target spectral trace. As with the SOSS observations, we apply a time-domain cosmic-ray detection due to the low number of groups.

We then apply the standard `ExoTDRFStage2`, including a new step, heavily based on the `Extract2DStep` within `rwst` (H. Bushouse et al. 2023) to extract the wavelength solution of the observations given the specific position of the target star within the NIRSpec slit. We then repeat the $1/f$ and background subtraction at the integration level, using the same parameters as the group-level subtraction, though we find that the addition of this step results in a negligible improvement to the noise properties of the final data frames. We also apply `ExoTDRF`'s principal-component-analysis-(PCA)-based `TracingStep` to NIRSpec data for the first time. This step reveals a subpixel drift in the y -position of the target trace over the course of the time series observations for both detectors and both visits, as well as a slight rotation about pixel (600, 15) for NRS1 and (500, 8) for NRS2. Finally, we locate the positions of the NRS1 and NRS2 spectral traces using the `edgetrigger` algorithm (M. Radica et al. 2022) and extract the stellar spectra using a box aperture extraction with a width of 8 pixels around the target trace.

2.2.2. Eureka! Reduction

Eureka! is an open-source pipeline for reducing and analyzing JWST and HST exoplanet transit, eclipse, and phase curve observations (T. J. Bell et al. 2022).²³ It has been extensively applied to JWST observations (see, e.g., E. M. Ahrer et al. 2023; S. E. Moran et al. 2023; S. Zieba et al. 2023; T. G. Beatty et al. 2024; Q. Xue et al. 2024).

Starting with the uncalibrated fits files, we first run Eureka!'s Stages 1 and 2, which are wrappers around the regular `rwst` pipeline and allow for changes as well as additions before running individual steps. We opted to use this capability to remove $1/f$ noise before the groups are combined into integrations by conducting a mean column-by-column background subtraction. Conducting a background subtraction at the group level has shown significant improvement in the noise properties for NIRSpec/G395H observations (e.g., L. Alderson et al. 2023).

Eureka!'s Stage 3 extracts the individual stellar spectra from each frame. First, we performed an outlier rejection with a 3σ rejection threshold along the time axis on the full frame. We then corrected for the curvature of the spectral trace and subtracted the background using the weighted mean value of each column, masking 10 times the median as outliers, and using a background region that is 6 pixels from the center of the

²² <https://jwst-docs.stsci.edu/>

²³ <https://github.com/kevin218/Eureka>

trace. Finally, we extracted the spectra within an aperture half-width of 4 pixels. In Stage 4, we generated light curves for each NRS1 and NRS2 and calculated stellar limb darkening for each bin using `ExoTiC-LD` (D. Grant & H. Wakeford 2024) and the `1D MPS-ATLAS` library (N. Kostogryz et al. 2023), using the stellar parameters in Table 1.

3. Light-curve Analysis

3.1. Joint White Light-curve Fitting

In order to obtain the most accurate possible orbital solution for GJ 3090 b, we jointly fit the light curves produced by `exoTEDRF` from all four visits. That is, we jointly fit a total of eight light curves: the first- and second-order white light curves from each of the two NIRISS/SOSS visits and the NRS1 and NRS2 light curves from each NIRSpec visit. For SOSS, we construct the order 1 white light curve by summing all the extracted flux, whereas we only consider wavelengths from 0.6 to 0.85 μm for order 2 (e.g., L. Albert et al. 2023; A. D. Feinstein et al. 2023; M. Radica et al. 2023, 2024; M. Fournier-Tondreau et al. 2024). For NIRSpec, we use wavelengths $\lambda \in [2.8, 3.7] \mu\text{m}$ and $\lambda \in [3.8, 5.1] \mu\text{m}$ for NRS1 and NRS2, respectively (e.g., L. Alderson et al. 2024).

We use the same general methodology as M. Radica et al. (2024) for the joint fit and employ the flexible light-curve fitting library `exoUPRF`²⁴ (M. Radica 2024b). The full light-curve model consists of two components: an astrophysical model and a systematics model. For the astrophysical model, we use a classic `batman` (L. Kreidberg 2015) transit model. The achromatic orbital parameters (the midtransit time, T_0 ; orbital period, P ; orbital eccentricity, e ; scaled semimajor axis, a/R_* ; and orbital inclination, i) are shared between all eight light curves. Chromatic parameters (scaled planet radius, R_p/R_* , two parameters of the quadratic limb-darkening law) are fit to both light curves of a given order or detector (i.e., a single value of R_p/R_* is fit to both SOSS order 1 white light curves). We fix the orbital period to 2.8531054 days (J. M. Almenara et al. 2022) and use wide, uninformative priors for all other parameters, except for the eccentricity, for which we put an upper bound at 0.32 (based on the 3σ upper limit in J. M. Almenara et al. 2022—though see Appendix A for the impacts of different assumed eccentricities). We also test freely fitting the orbital period but find a value exactly in agreement with but marginally less precise than that determined by J. M. Almenara et al. (2022).

The systematics models handle everything else in the light curves that is not the planet’s transit. For each light curve, the optimal systematics model is determined by comparing the Bayesian information criterion. For SOSS, in addition to a linear slope fit independently to each order and each visit, we also linearly detrend against the beating pattern picked up by the PCA and commonly seen in SOSS observations (e.g., L. Albert et al. 2023; L.-P. Coulombe et al. 2023; C. Cadieux et al. 2024; M. Radica et al. 2024). In order to handle the ~ 100 ppm amplitude-correlated noise that is visible by eye in the transit baseline, we also include a Gaussian process (GP) for each visit using a Matérn 3/2 kernel as implemented by `celerite` (D. Foreman-Mackey et al. 2017). We share the GP timescale between both orders but fit the GP amplitude

separately (e.g., M. Radica et al. 2024). Moreover, we train the GP on the y -position of the spectral trace, as determined through the PCA performed by `exoTEDRF`, as we find that this performs better than a GP with time in removing residual correlated noise.

For NIRSpec, the systematics model consists of a linear slope (e.g., L. Alderson et al. 2023; S. E. Moran et al. 2023; N. L. Wallack et al. 2024) with time that we fit independently to each detector and each visit. For visit 2, we also include a GP with time, again using the Matérn 3/2 kernel. Since the correlated noise structures are consistent between the two detectors, we share the characteristic frequency between NRS1 and NRS2 but fit the GP amplitude separately to each. In visit 1, the pretransit baseline was plagued by large systematics, which we were not able to adequately correct. We therefore cut the first 1000 integrations for the NRS1 and NRS2 light curves for NIRSpec visit 1. Moreover, there was a clear flare just after midtransit during the second NIRSpec visit. Flares have proven to be nontrivial to model in-transit light curves (e.g., W. S. Howard et al. 2023; O. Lim et al. 2023; M. Radica et al. 2025), and after several attempts to fit the flare (see Appendix B), we opt to simply mask the affected integrations (integrations 1810–2160). Figure E1 shows the NRS2 light curves for both visits without any integrations cut.

Finally, for each light curve (both NIRISS and NIRSpec), we include an error inflation term added in quadrature to the flux error. As with the astrophysical model, we use wide, uninformative priors for each parameter. Our total model, therefore, has 54 free parameters. We explore the posterior space with `emcee` (D. Foreman-Mackey et al. 2013), using 110 chains and 100,000 steps per chain, the first 80% of which we discard as burn-in. The light curves and best-fitting models for each instrument and visit are shown in Figure 2, and the constraints on the most relevant parameters are presented in Table 2.

3.2. Spectroscopic Light-curve Fitting

3.2.1. NIRISS/SOSS

For the `exoTEDRF` light curves, we continued to use `exoUPRF` and binned the light curves to $R = 100$ before fitting in order to increase the signal-to-noise ratio and better handle the substantial systematics. We fixed the orbital parameters to the values in Table 2 and left the scaled planet radius free. We freely fit the two parameters of the quadratic limb-darkening law in the range $u_1, u_2 \in [-1, 1]$. For the systematics model, we detrended against the linear slope with time and beating pattern. We also included the additive error inflation term and the GP model, where we fixed the GP timescale to the best-fitting value from the white light-curve fit and allowed the amplitude to vary freely for each wavelength bin. This has proved to be an effective method to remove correlated noise when the noise structures do not vary strongly with wavelength (e.g., M. Radica et al. 2024). We followed this same prescription for both visits. The posterior exploration was carried out using the dynamic nested sampling implemented through `dynesty` (J. S. Speagle 2020) using 1000 live points. The final `exoTEDRF` NIRISS/SOSS transmission spectra for both visits (which we treat as our fiducial spectra for the remainder of the analysis) are shown in Figure 3. Note that the two spectra show differences (e.g., offset and slope) that are discussed in detail in Section 5.

²⁴ <https://github.com/radicamc/exoUPRF>

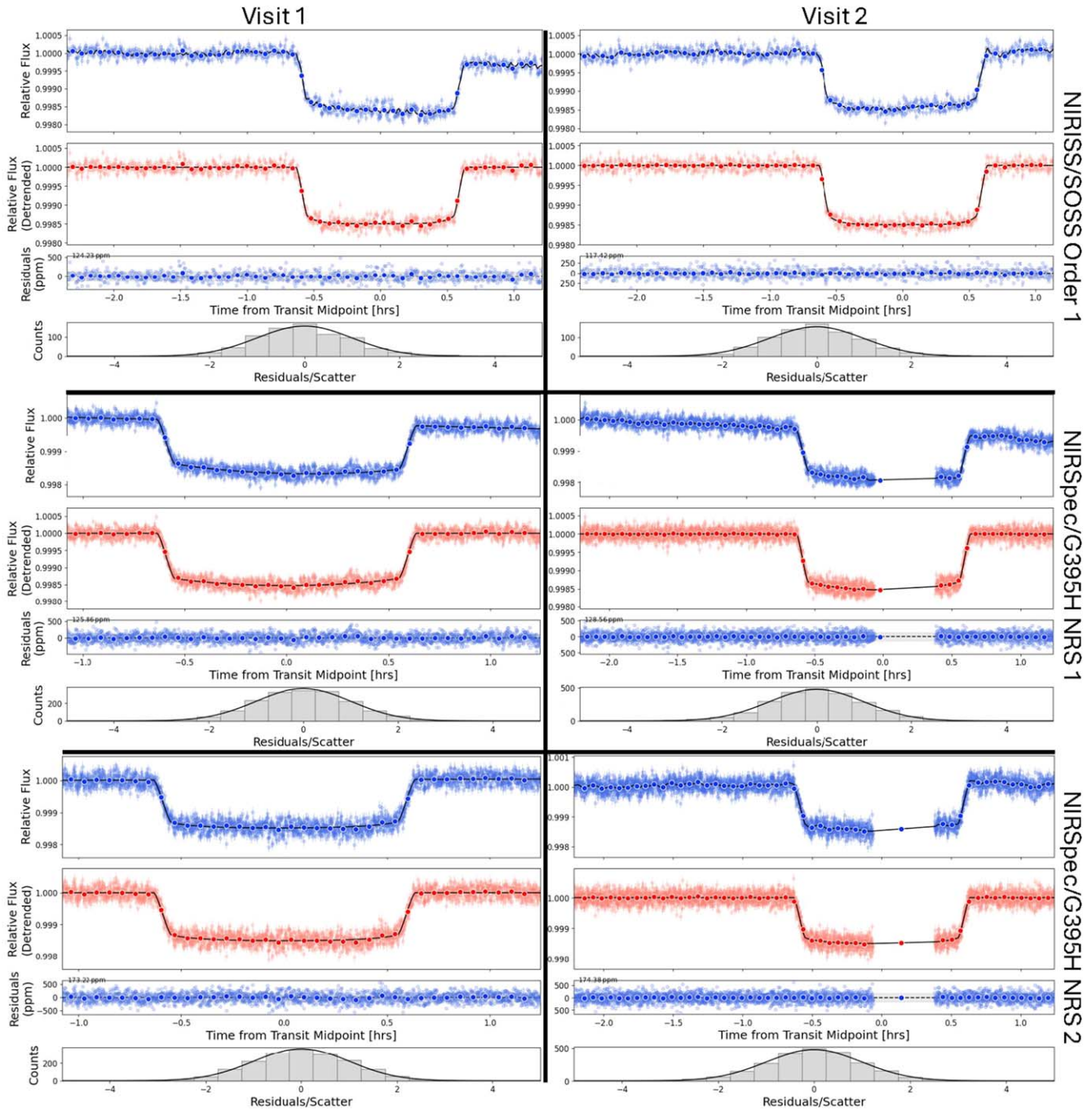


Figure 2. Results of the joint white light-curve fitting. In each of the six panels, the first row shows the raw white light curve in blue, with the best-fitting model overlotted in black. The second row shows the systematics-corrected white light curve, with the best-fitting astrophysics model in black. The third row shows the fit residuals, and the bottom row shows the histogram of the residuals. In the outer grid, the first column of panels corresponds to the first visit with each instrument and the second column to the second visit. The first row of panels shows the order 1 white light curves from NIRISS/SOSS. Note that NIRISS/SOSS order 2 is left out in this figure as it is much noisier compared to order 1 but shows similar systematics. The second and third rows are the NIRSpec/G395H white light curves for the NRS1 and NRS2 detectors, respectively. Note that integrations around the flare have been masked in both detectors of the second NIRSpec visit, and the first 1000 integrations of NIRSpec visit 1 are cut to remove large amounts of correlated noise. The raw, uncut NIRSpec light curves are shown in Figure E1.

For fitting the NAMELESS spectroscopic light curves, we used the Tiberius pipeline fitting stage (J. Kirk et al. 2017, 2021)²⁵ with the nested sampling algorithm PolyChord (W. J. Handley et al. 2015a, 2015b) adaption (E. Ahrer et al. 2022). In both visits, we used a spectral resolution of $R=100$ for the binning of the light curves. The system parameters were fixed to the retrieved values from the joint

white light analysis in Table 2, but we left the transit depth free as well as the limb-darkening parameters u_1 , u_2 using the quadratic limb-darkening law and a large uninformative prior range (e.g., see L.-P. Coulombe et al. 2024). To detrend our light curves, we also fitted for a linear trend in time, a linear dependency on the beating pattern (PCA component), and a noise multiplying factor to account for any additional white noise. Contrary to the *exoTEDRF* light-curve fitting, we did not include a GP model to fit our NAMELESS light curves. The

²⁵ <https://github.com/JamesKirk11/Tiberius>

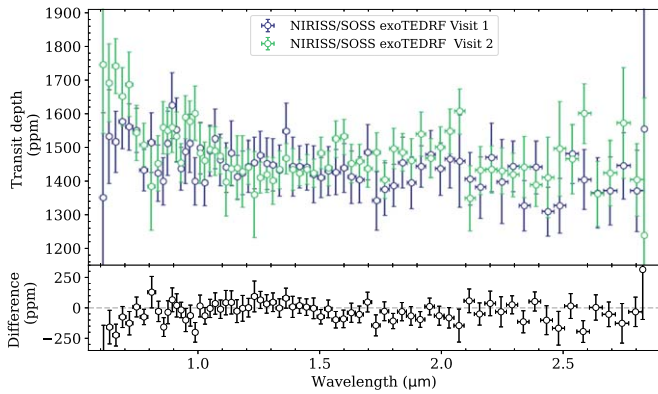


Figure 3. exoTEDRF transmission spectra of GJ 3090 b from both NIRISS/SOSS visits. Visit 1 is displayed in blue and visit 2 in light green, and the differences between them are shown in the bottom panel in black.

Table 2

Retrieved Planetary Parameters from the Joint Light-curve Fitting of the Four Transits of GJ 3090 b

Parameters	Fitted Value
Midtransit time, T_0 (MJD _{TDB})	$60158.812806 \pm 0.000074$
Planet-to-star radius ratio, R_p/R_*	
NIRISS/SOSS order 1	$0.03789^{+0.00044}_{-0.00038}$
NIRISS/SOSS order 2	$0.03911^{+0.00046}_{-0.00047}$
NIRSpec/G395H NRS1	$0.03878^{+0.00025}_{-0.00021}$
NIRSpec/G395H NRS2	$0.03835^{+0.00023}_{-0.00020}$
Semimajor axis, a/R_*	12.96 ± 0.63
Inclination, i	86.86 ± 0.35
Eccentricity, e	$0.057^{+0.072}_{-0.041}$

NAMELESS transmission spectra are in excellent agreement with the fiducial exoTEDRF spectra, as can be seen in Appendix Figure E2.

Despite the large differences in transit depth uncertainties, we ultimately select the exoTEDRF reduction as our fiducial spectra for two reasons: first, to have consistently reduced and fit spectra across our entire NIRISS and NIRSpec wavelength range, and second, as we believe the larger error bars on the exoTEDRF SOSS spectra (most likely introduced through the use of a GP) compared to the NAMELESS spectra better encapsulate the uncertainties in the measured transit depths due to the significant amounts of correlated noise visible in the light curves.

3.2.2. NIRSpec/G395H

For the exoTEDRF spectra, we followed the same procedure as outlined above for SOSS, except we altered the systematics models as befitted the NIRSpec observations. For visit 1, the systematics model consisted of a linear slope with time and the additive error inflation term. For visit 2, we also include the GP model, but unlike with SOSS, we freely fit both the amplitude and timescale to each bin as the correlated noise structures displayed some variations with wavelength. We again show the final transmission spectra for each visit in Figure 4. The two spectra from the two visits show some differences, especially in the redder wavelength ranges, where the signal-to-noise is lower. However, we have not found evidence that the two visits are statistically different (at 1σ , $>68\%$ agreement), which would prohibit a combined analysis. We focus on results from

the exoTEDRF spectra in the remainder of the analysis in order to have a consistently reduced and fit spectrum.

For our Eureka! reduction of the NIRSpec data, we also fit the light curves using Eureka!’s Stage 5. Again we fixed all system parameters according to our joint white light analysis (Table 2). For the limb darkening, we used the quadratic limb-darkening law and left u_2 free, while we fixed u_1 to the generated value from Stage 4 (ExoTiC-LD; MPS-ATLAS; N. Kostogryz et al. 2023; D. Grant & H. Wakeford 2024) to avoid degeneracy, but we also investigated leaving both u_1 and u_2 free, which did not change our retrieved transmission spectrum. Therefore, the fiducial model for spectroscopic light-curve fitting using the NIRSpec data consists of the transit model using the parameters R_p/R_* , u_2 and a linear trend in time, as well as a white noise parameter in the form of a multiplier. In the case of visit 2, we also added a GP model to account for the additional variability seen in the light curves. We freely fit the GP covariance amplitude for each spectroscopic light curve but fix the length scale to the value obtained when fitting the white light curve. Again, we compare the Eureka! NIRSpec/G395H transmission spectra with the fiducial exoTEDRF ones in Appendix Figure E2.

4. Analysis of the Metastable He I Triplet

NIRISS/SOSS has wavelength coverage that includes the metastable He I triplet at $1.0833 \mu\text{m}$, a tracer of escaping H_2/He atmospheres. For this reason, we also compute a transmission spectrum of GJ 3090 b at pixel-level resolution for our two visits with SOSS using both the exoTEDRF pipeline and NAMELESS to better observe this narrow feature. Figure 5 shows the spectra for both visits using our fiducial exoTEDRF reduction.

As we do not expect to resolve the He line shapes, we use simple Gaussian and Lorentzian models to investigate three fitting scenarios using both pixel-level spectra simultaneously and the nested sampling algorithm *dynesty* (J. S. Speagle 2020) to quantify the He detection: (1) a Gaussian function with a full width at half-maximum (FWHM) equal to the resolution of NIRISS/SOSS ($R \sim 650$ at $1.083 \mu\text{m}$) centered on the helium triplet with three free parameters (offset, slope, and amplitude), under the assumption that the individual lines of the He triplet do not contribute to the shape of the observed absorption; (2) Lorentzian helium line profiles convolved with the instrumental resolution with four free parameters (offset, slope, amplitude, and He line width); and (3) a flat line with two free parameters (offset and slope)—i.e., a null result for He detection. Note that model 2 is just a simple test of whether the He absorption is significantly broadened beyond the instrumental resolution.

Using the exoTEDRF reduction, we find that model 1 is favored over model 2, with $\Delta \log(\mathcal{Z}) \sim 2.5$; i.e., there is no indication that the width of the feature needs to be modeled with more than the instrumental resolution element. This is supported by running the identical analysis on the NAMELESS reduction, where we find a Bayesian evidence difference of $\Delta \log(\mathcal{Z}) \sim 1.2$ in favor of model 1.

Moreover, the flat line (model 3) is rejected compared to the Gaussian (model 1) by a Bayesian evidence difference of $\Delta \log(\mathcal{Z}) = 12.8 \pm 0.2$ for exoTEDRF and $\Delta \log(\mathcal{Z}) = 15.8 \pm 0.2$ for NAMELESS. This shows that the Gaussian helium model is preferred to a flat line at $\sim 5.5\sigma$ significance (exoTEDRF) and $\sim 5.9\sigma$ significance (NAMELESS). The best-

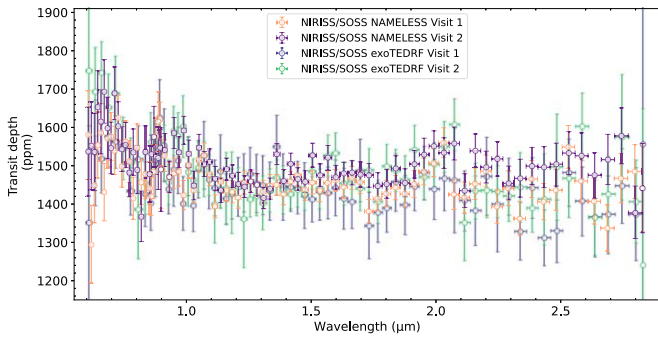


Figure 4. exoTEDRF transmission spectra of GJ 3090 b from both NIRSpec/G395H visits. Visit 1 is displayed in the dark blue color and visit 2 in the light green color, and the differences between them are shown in the bottom panel in black.

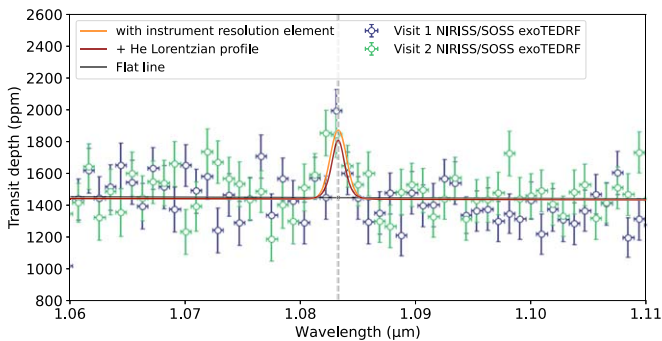


Figure 5. Pixel-level NIRISS/SOSS transmission spectrum of GJ 3090 b using the exoTEDRF pipeline in the wavelength range surrounding the He I triplet (gray dashed line). Our best fits to the data via three model considerations are (1) a Gaussian model of the He lines with a width dictated by the instrument resolution (orange), (2) a Gaussian for the instrument response convolved with the helium triplet line profiles treated as Lorentzians (dark red), and (3) a flat line (black).

fit amplitudes from both reductions are 435 ± 79 ppm (exoTEDRF) and 460 ± 77 ppm (NAMELESS), entirely consistent with each other and $>5\sigma$ inconsistent with 0. This result marks the first detection of escaping helium from a sub-Neptune with JWST.

We further use a Gaussian model with a fixed width (0.75 \AA) convolved at the resolution of NIRISS/SOSS to provide an estimate of the resolved helium signature as seen at high spectral resolution (e.g., M. Fournier-Tondreau et al. 2024; C. Piaulet-Ghorayeb et al. 2024; M. Radica et al. 2024). The best-fit value for the helium absorption amplitude expected at high resolution (convolved at $R \sim 100,000$) is $1.0\% \pm 0.2\%$. This is in reach of current high-resolution spectrographs such as NIRPS (F. Bouchy et al. 2017) in three to four transits for robust detection and interpretation of the helium line shape.

We then proceed to confirm that the He signal is stable throughout the whole transit and is not only produced during a fraction of it. We use the light curves at the pixel resolution of NIRISS/SOSS for the 47 pixels around the helium line (centered at $1.083 \mu\text{m}$), covering the $1.062\text{--}1.105 \mu\text{m}$ wavelength range. Each light curve is first normalized by its average out-of-transit flux. A baseline white light curve surrounding the helium triplet is then generated by averaging all the light curves (a total of 38) from 1.062 to $1.078 \mu\text{m}$ and from 1.088 to $1.105 \mu\text{m}$. The helium light curve is then computed by dividing

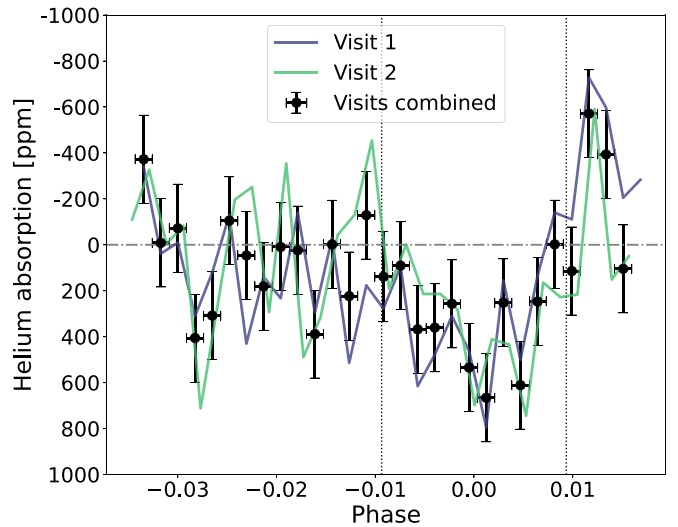


Figure 6. NIRISS/SOSS relative helium light curve showing clear absorption during the transit for visit 1 (dark blue) and visit 2 (light green) and the two visits combined (black). The transit ingress and egress are marked with the vertical dotted lines. The relative light curve was computed by dividing the light curve that includes the He triplet by the average of the surrounding light curves (from 1.062 to $1.078 \mu\text{m}$ and from 1.088 to $1.105 \mu\text{m}$).

the light curve covering the $1.083 \mu\text{m}$ He triplet by the previously produced white light curve. We show the results in Figure 6 for both visits as well as the two combined. We find clear absorption of ~ 500 ppm during the whole transit. With the relatively short baseline at hand, no significant absorption is measured pre- and/or posttransit that could have traced an atmospheric escape tail.

5. Atmosphere and Stellar Contamination Modeling

5.1. Methodology

The NIRISS spectra display $150\text{--}200$ ppm slopes toward short wavelengths, especially shortward of $\sim 1.1 \mu\text{m}$ (Figure 3), and are also systematically shifted up compared to the NIRSpec spectra (from both visits) by ~ 95 ppm. We were unable to trace this back to inconsistent system parameters used during light-curve fitting, limb-darkening choices, or any specific choices made during the data reduction (e.g., bias scale, outlier rejections, aperture size, background subtraction method). Instead, we interpret these features as telltale signs of unocculted stellar heterogeneities, with time-varying properties that result in offsets between the NIRISS and NIRSpec spectra and even between the two NIRISS spectra.

The distributions of heterogeneities on stellar surfaces, and therefore the impacts of stellar contamination on transmission spectra in the form of the transit light source (TLS) effect (B. V. Rackham et al. 2018, 2019), are not constant in time. There is a significant time gap between the NIRISS and NIRSpec observations compared to the stellar rotation period, as well as between individual visits with NIRISS, meaning that we cannot reasonably assume that the distribution of spots and faculae on GJ 3090, and thus the impacts of the TLS effect, will be the same in one visit compared to another. The differing behavior of the NIRISS spectra at the shortest wavelengths, as well as the offsets between the NIRISS and NIRSpec spectra, also support this point.

In light of the impacts of the TLS effect, the most conservative approach would be to jointly fit the spectra from

Table 3

Constraints on the Stellar Contamination Parameters Affecting the NIRISS/SOSS Transmission Spectrum for Free Retrievals

Parameter	POSEIDON	SCARLET	Aurora
NIRISS Visit 1			
$T_{\text{phot,star}}$ (K)	$3564.14^{+54.62}_{-56.57}$	$3556.17^{+67.33}_{-69.22}$	$3564.48^{+80.37}_{-84.87}$
T_{spot} (K) ^a	$2960.64^{+345.03}_{-301.51}$	$2964.61^{+320.89}_{-259.97}$	$2839.66^{+413.39}_{-373.06}$
f_{spot} (K)	$0.12^{+0.05}_{-0.06}$	$0.14^{+0.07}_{-0.06}$	$0.10^{+0.05}_{-0.05}$
Order 2 offset	...	$-17.83^{+31.82}_{-30.97}$	$-23.73^{+30.6}_{-32.36}$
NIRISS Visit 2			
$T_{\text{phot,star}}$ (K)	$3575.31^{+52.32}_{-49.54}$	$3591.1^{+62.25}_{-62.61}$	$3612.62^{+73.9}_{-71.95}$
T_{spot} (K) ^a	$3223.19^{+94.3}_{-129.71}$	$3194.19^{+84.84}_{-103.26}$	$3195.61^{+101.87}_{-110.89}$
f_{spot} (K)	>0.23	>0.31	>0.31
Order 2 offset	...	$69.87^{+31.19}_{-32.48}$	$105.29^{+36.33}_{-35.15}$

Notes. Including both stellar heterogeneities and the planetary atmosphere contribution. Retrievals were applied to both visits separately using SCARLET, POSEIDON, and Aurora. Lower limits reported are 2σ .

^a For the SCARLET retrieval, derived from the samples on T_{phot} and ΔT_{spot} .

all four visits, assuming the same underlying planetary atmosphere and different TLS realizations for each. However, this level of complexity is currently out of reach of most modeling codes. Therefore, we take a step-by-step approach and fit the two NIRISS visits separately, as well as NIRSpec separately from NIRISS.

For NIRISS/SOSS, we find the spectra to be entirely dominated by the effects of stellar contamination (see Section 6.1 and Appendix C.2) and thus explore the properties of the stellar heterogeneities that give rise to the observed features. Particularly, given that the two NIRISS visits are separated by >200 days, we explore the differences between the properties of the stellar surface at these two epochs. With NIRSpec/G395H, however, we do not find strong evidence that the spectra are affected by stellar contamination. Therefore, we combine the spectra from the two visits via a weighted average in order to probe the properties of the planetary atmosphere.

5.2. Overview of Models

We use SCARLET, POSEIDON, and AURORA to perform 1D atmosphere retrievals on both the NIRISS/SOSS and NIRSpec/G395H spectra, accounting for the potential impact of unocculted stellar surface heterogeneities as well as degeneracies between stellar and planetary properties. Specifically, we perform stellar heterogeneity-only (described in more detail in Appendix C.2) and joint planet atmosphere–stellar heterogeneity retrievals on the NIRISS/SOSS data, whereas for the NIRSpec/G395H data, we perform planet-atmosphere-only retrievals and combined atmosphere–stellar heterogeneity retrievals using either free chemistry or chemically consistent compositions. Finally, we put our atmosphere results in context using self-consistent chemical equilibrium and disequilibrium forward model grids. For each retrieval code, inferences on the stellar photosphere from NIRISS are presented in Table 3, and constraints on the planet atmosphere from NIRSpec are shown in Figure D1.

5.2.1. Atmosphere-only and Joint Retrievals

Aurora. We perform flexible “free” retrievals using Aurora (L. Welbanks & N. Madhusudhan 2021). With

Aurora, a transmission spectrum is generated based on a model parameterized by constant-with-altitude molecular gas volume mixing ratios (H_2O , CH_4 , CO_2 , SO_2 , H_2S), an isothermal vertical temperature profile, cloud properties following the two-sector prescription from L. Welbanks & N. Madhusudhan (2021) using the linear combination approach from M. R. Line & V. Parmentier (2016), and the reference radius at a reference pressure (L. Welbanks & N. Madhusudhan 2019). Gases included are selected based on those expected in warm atmospheres and with cross sections described in previous works (S.-M. Tsai et al. 2022; L. Welbanks et al. 2024). We additionally retrieve the impact of stellar heterogeneities through the TLS effect following the description of A. Pinhas et al. (2018) as implemented in L. Welbanks & N. Madhusudhan (2021). We consider both hydrogen-rich and secondary atmospheres by using the center-log-ratio transformation as described in L. Welbanks & N. Madhusudhan (2021) and scenarios where H and He in a solar mixture (M. Asplund et al. 2009) are the background gas of the planet atmosphere. Additionally, we allow for the possibility of instrumental offsets between both NIRSpec detectors and between NIRISS orders.

Aurora estimates planet parameters using PyMultiNest nested sampling (J. Buchner et al. 2014) and 2000 live points. Models assume a 1D hydrostatic equilibrium atmosphere spanning pressures of 10^{-9} – 10^2 bars in 100 uniformly spaced layers in logarithmic pressure space. The model performs line-by-line opacity sampling at a spectral resolution of 20,000 and then bins the spectrum down to the resolution of the observations. Our fiducial case for the NIRSpec observations has 13 free parameters: five molecules, one for an isothermal pressure–temperature profile, four for inhomogeneous clouds and hazes, one for the radius of the planet at the one reference pressure parameter, and one for the instrumental offset between NRS1 and NRS2.

POSEIDON. We perform an additional independent atmospheric retrieval analysis using the open-source retrieval code POSEIDON (R. J. MacDonald & N. Madhusudhan 2017; R. J. MacDonald 2023). POSEIDON makes use of 2000 PyMultiNest live points in all of our retrievals, a nested sampling algorithm used for our parameter estimation, and model comparison (F. Feroz et al. 2009; J. Buchner et al. 2014). A more comprehensive description of the radiative transfer technique and forward model (TRIDENT) used by POSEIDON and its corresponding opacity database can be found in R. J. MacDonald & N. K. Lewis (2022). Using the exoTEDRF reductions of the NIRISS/SOSS and NIRSpec/G395H data sets specified in Section 2.1.1, we generate model spectra from both 0.6 to 2.9 μm and 2.9 to 5.3 μm , respectively, at $R = 20,000$. This is convolved with a Gaussian kernel to the native resolution of each instrument and multiplied by the corresponding instrument sensitivity function so that it can then be binned to the desired wavelength spacing of each spectrum.

We include a wide array of atmospheric and stellar parameters in our retrievals of GJ 3090 b. In each of our retrievals, we fit for a reference radius $R_{\text{p,ref}}$ at a designated reference pressure of 10 bars. To account for the difference in observations between instruments and in order to compute detection significances, we conduct a combination of nested retrievals, including flat-line models and multigas models with or without stellar contamination (see Section 6.1) for both our NIRISS/SOSS and NIRSpec/G395H reductions. Our base

multigas atmospheric models include the gases H_2 , He, H_2O , CH_4 , CO_2 , SO_2 , CO, NH_3 , and H_2S , where H_2 and He are calculated as the background gas at a fixed He/ H_2 ratio of 0.17. Each of these models also includes clouds and hazes, where we utilize a two-parameter ($\log a_{\text{haze}}$ and γ) power-law prescription for hazes (R. J. MacDonald & N. Madhusudhan 2017). We assume an optically thick gray opacity, in which all cloud layers deeper than P_{surf} are set to infinite opacity in our retrievals. We also assume both a fixed surface gravity of the stellar regions of $\log g = 4.727 \pm 0.029$ (cgs; J. M. Almenara et al. 2022) and an isothermal atmospheric temperature for our models. The priors for each of our models of GJ 3090 b are specified as the following: $R_{p,\text{ref}} (R_{\oplus}) = \mathcal{U}(1.28, 2.45)$, $T \text{ (K)} = \mathcal{U}(100, 1000)$, $\log a_{\text{haze}} = \mathcal{U}(-4, 8)$, $\gamma_{\text{haze}} = \mathcal{U}(-20, 2)$, $\log P_{\text{cloud}} = \mathcal{U}(-7, 2)$, and $\log X = \mathcal{U}(-12, 0)$.

We additionally utilize POSEIDON to determine the extent of the TLS effect on the NIRISS spectra of GJ 3090 b. POSEIDON accounts for stellar contamination by multiplying a bare-rock transmission term, $(R_p/R_*)^2$, by the wavelength-dependent stellar contamination factor from two discrete stellar heterogeneities (spots and faculae). POSEIDON creates the model spectra of the active stellar regions by utilizing the PYMSG package, through which POSEIDON interpolates across the PHOENIX grid of stellar atmosphere models (T.-O. Husser et al. 2013). We include five extra free parameters in addition to the aforementioned parameters in these models: $f_{\text{fac}} = \mathcal{U}(0.0, 0.5)$, $f_{\text{spot}} = \mathcal{U}(0.0, 0.5)$, $T_{\text{fac}} \text{ (K)} = \mathcal{U}(T_* - 36, 1.2T_*)$, $T_{\text{spot}} \text{ (K)} = \mathcal{U}(2300, T_* + 36)$, and $T_{\text{phot}} \text{ (K)} = \mathcal{U}(T_*, 12)$, where $T_* = 4236 \pm 12$. This results in a total of 16 free parameters tested in both our NIRSpec and NIRISS retrievals of GJ 3090 b.

We lastly use POSEIDON to conduct several Bayesian comparisons between the different models delineated above for both NIRISS and NIRSpec. To provide more robust Bayesian comparisons between our atmosphere models and every other nested model, we construct additional “minimal atmosphere” models. These models limit the number of atmospheric free parameters by getting rid of any completely unconstrained molecules. For our NIRISS minimal atmosphere models, we include CO_2 , SO_2 , CO, and H_2S , while for our corresponding NIRSpec models, we include CO_2 , SO_2 , and CO. Allowing the cloud-top pressure ($\log P_{\text{cloud}}$) to vary, this results in nine free parameters in our NIRISS minimal atmosphere model (12 when starspots are jointly included) and eight free parameters in our NIRSpec minimal atmosphere model (11 with starspots).

SCARLET. We also perform retrievals with SCARLET to test other assumptions not supported by other codes (e.g., fitting shared atmosphere properties and visit-specific TLS parameters to the NIRISS/SOSS spectra) for free retrievals and to put the results from the free retrievals in context with a further exploration involving chemically consistent retrievals. We use a version of SCARLET (B. Benneke & S. Seager 2012, 2013; B. Benneke 2015; B. Benneke et al. 2019a, 2019b; S. Pelletier et al. 2021) adapted for observations of sub-Neptunes with JWST (C. Piaulet et al. 2023; C. Piaulet-Ghorayeb et al. 2024) to perform retrievals on the transmission spectra of GJ 3090 b.

In our forward-modeling framework for free retrievals, the molecular abundances are assumed to be constant with altitude in the atmosphere. For chemically consistent retrievals, the chemistry is dictated by chemical equilibrium in each atmospheric layer given the local temperature and pressure conditions and parameterized by the C/O ratio and metallicity

of the atmosphere. We explore the presence of higher SO_2 abundances than predicted in equilibrium (e.g., T. G. Beatty et al. 2024) by performing retrievals where the chemical equilibrium SO_2 abundance is overwritten by a vertically constant abundance profile with the abundance as a free parameter (while the other molecular abundances are scaled to keep the total equal to unity).

Since transmission spectra are largely insensitive to the temperature profile, we either assume that it is an isotherm (where the temperature fitted in the retrieval is representative of the planet’s photosphere at the terminator) or parameterize it following N. Madhusudhan & S. Seager (2009) in order to assess the sensitivity of our retrieved abundances to the choice of T-P profile parameterization. For the set T-P profile and abundances, we compute the atmospheric structure in hydrostatic equilibrium and the radiative transfer calculation for the slant transmission geometry.

For each model evaluation within the Bayesian retrieval framework, we use `scipy.minimize` to fit the radius at a pressure of 10 mbar in our atmosphere model that provides the best match to the observed spectrum (iterating over the hydrostatic equilibrium and radiative transfer steps for each test radius for consistency). Our baseline free retrievals include H_2 , He, H_2O , CO, CO_2 , CH_4 , HCN, H_2S , SO_2 , and NH_3 , but we perform a few retrievals with only a subset of these molecules to assess Bayesian detection significances (R. Trotta 2008; B. Benneke & S. Seager 2013). We assume a mix of H_2 and He as the filler gas, with a Jupiter-like He/ H_2 ratio of 0.157 (U. von Zahn & D. M. Hunten 1996). Our opacities are computed from the HELIOS-K (S. L. Grimm & K. Heng 2015) cross sections for H_2O (O. L. Polyansky et al. 2018), CO (R. J. Hargreaves et al. 2019), CO_2 (S. N. Yurchenko et al. 2020), CH_4 (R. J. Hargreaves et al. 2020), HCN (G. J. Harris et al. 2006), H_2S (A. A. A. Azzam et al. 2016), SO_2 (D. S. Underwood et al. 2016), and NH_3 (P. A. Coles et al. 2019). For the baseline model, we parameterize clouds as a gray opacity source with the cloud-top pressure p_{cloud} fitted in the retrieval. We also fit the cloud covering fraction f_{cloud} as implemented in C. Piaulet-Ghorayeb et al. (2024) to account for potential patchy cloud coverage. To account for the potential impact of small-particle hazes on our spectrum, we parameterize them using the slope enhancement parameter c_{haze} that multiplies the Rayleigh scattering slope. Beyond planetary parameters, we account for potential instrument offsets between orders 1 and 2 of NIRISS/SOSS, between the spectra obtained from the first and second NIRISS/SOSS visits, and between the NRS1 and NRS2 detectors of NIRSpec/G395H.

We use the SCARLET implementation of `nestle`²⁶ (J. Skilling 2004, 2006) to sample the parameter space. We compute the models at a resolving power of 15,625 (or 31,250 for a higher-resolution test) and convolve them in each observed bandpass assuming uniform throughput for the likelihood evaluation.

Finally, for retrievals where we fit for the impact of both the planetary atmosphere and stellar heterogeneities on the observed transmission spectrum, we use the SCARLET implementation of TLS effect modeling, which leverages the MSG module to obtain stellar models (see C. Piaulet-Ghorayeb et al. 2024 for a description). For these joint retrievals, we simultaneously sample the parameters of the planetary

²⁶ <http://kylebarbary.com/nestle>

atmosphere and the stellar surface as parameterized in the `stctm` implementation. The stellar contamination factor $\epsilon_{\lambda, \text{het}}$ multiplies the predicted transmission spectrum given the sampled atmosphere parameters prior to the likelihood evaluation. We test cases where we consider no stellar contamination, spots only (with a single population having a shared T_{spot}), and both spots and faculae with an associated temperature contrast and covering fraction for each heterogeneity population. In this case, we use an updated version of SCARLET (C. Piaulet-Ghorayeb et al. 2025, in preparation) that supports the modeling of visit-specific stellar contamination signatures with a shared visit-independent planetary atmosphere composition.

5.2.2. Self-consistent Model Grids

SCCHIMERA. Finally, we estimate the atmospheric parameters of GJ 3090 b with “grid-based retrievals” using the atmosphere modeling code, SCCHIMERA. From a grid of precomputed models, we estimate planet parameters using Bayesian nested sampling following a process similar to L. Welbanks et al. (2024). Models are 1D, varying along a vertical pressure–temperature profile, and assume that the atmosphere thermal structure and composition are in radiative–convective–thermochemical equilibrium (1D-RCTE). The model grid includes a range of values for planet irradiation temperature ($T_{\text{irr}} = 550\text{--}700$ K in 25 K increments, a proxy for energy redistribution allowing for cooler temperatures near the day–night terminator), atmospheric carbon-to-oxygen ratio (C/O = 0.2–0.6 in 0.1 increments, although we did explore allowing C/O to extend up to 0.8 with a coarse grid prior to limiting C/O < 0.6), and atmospheric metallicity ($[M/H] = 2.5\text{--}4.5$ in 0.25 increments, in which M accounts for all non-H/He elements and $[\]$ denotes \log_{10} relative to solar ratios).

To produce each model, SCCHIMERA iteratively computes the pressure–temperature structure ($10^{-8}\text{--}10^2$ bars in $10^{0.2}$ bar layers) from an intrinsic temperature ($T_{\text{int}} = 100$ K; this choice does not impact the RCTE model at the low pressures probed by transmission observations) and the top-of-atmosphere incident stellar flux computed from a PHOENIX stellar model (T.-O. Husser et al. 2013; $T_{\text{star}} = 3556$ K, $\log(g)(\text{cgs}) = 4.727$). Then, the NASA CEA2 routine for Gibbs free energy minimization (S. Gordon & B. J. McBride 1994) solves the equilibrium gas volume mixing ratios of thousands of molecular/atomic species along the pressure–temperature profile. We include opacity sources for major radiative species: H₂–He collision-induced absorption, H/e[−]/H[−] bound–/free–free continuum, and the line opacities for H₂O, CO, CO₂, CH₄, NH₃, H₂S, PH₃, HCN, C₂H₂, OH, TiO, VO, SiO, FeH, CaH, MgH, CrH, ALH, Na, K, Fe, Mg, Ca, C, Si, Ti, O, Fe⁺, Mg⁺, Ti⁺, Ca⁺, and C⁺ (for details of line sources, see M. Mansfield et al. 2021; A. R. Iyer et al. 2023).

To estimate the properties of GJ 3090 b, we use Bayesian nested sampling with PyMultiNest (J. Buchner et al. 2014). We allow for 500 live points within the grid parameter space (T_{irr} , [M/H], and C/O) and trilinearly interpolate the temperature structure and gas mixing ratio profiles between grid models. During this parameter estimation stage, we compute transmission spectra with the addition of a vertically uniform gray cloud opacity (κ_{cloud}) postprocessed onto the spectrum, a cloud covering fraction, an instrument offset allowing the NRS1 transit depth to move up/down, and a multiplier on

Table 4
Chemically Consistent Retrieval (SCARLET) and Grid Constraints on the Atmospheric Composition of GJ 3090 b

Parameter	SCCHIMERA Eq. Grid	SCCHIMERA Diseq. Grid	SCARLET Eq. Retrieval
Met. [\times solar]	>1348	>1230	>776
C/O	< 0.43	< 0.54	<0.42
$\times R_p$	0.99 ± 0.01	0.99 ± 0.01	0.99 ± 0.01

Note. From the $R = 100$ version of the exoTDRF NIRSspec/G395H visit 1+2 spectrum. We only report constraints on the parameters that were meaningful to explain the data from a Bayesian model comparison standpoint. The “grid-trial” results were obtained with SCCHIMERA using chemical and disequilibrium grids. Free parameters in the grid not reported here (T , κ_{cloud} , and cloud covering fraction) were unconstrained. Upper and lower limits are 2σ , except for C/O reported from the SCCHIMERA grid-based retrievals. C/O is unconstrained by SCCHIMERA, but we report the 1σ preference.

planet radius ($\times R_p$). Overall, we include free parameters for T_{irr} , [M/H], C/O, κ_{cloud} , cloud covering fraction, instrument offset, and $\times R_p$. We report constraints on [M/H], C/O, instrument offset, and $\times R_p$ in Table 4. The remaining parameters are unconstrained.

To test the impact of disequilibrium chemistry due to vertical mixing and photochemistry, we additionally processed models using the VULCAN kinetics code (S.-M. Tsai et al. 2017), following the process in L. Welbanks et al. (2024). This disequilibrium model grid spans a smaller parameter space than the 1D-RCTE grid, including only models with C/O = 0.4, 0.5, and 0.6. We assume a vertically constant K_{zz} profile, $K_{zz} = 10^9 \text{ cm}^2 \text{ s}^{-1}$, and use the UV-stellar spectrum of GJ 832 (A. Youngblood et al. 2016) as a proxy for GJ 3090. We adopt a zenith angle of 83° for the terminator region following S. M. Tsai et al. (2023). With the introduction of vertical mixing, T_{int} does influence the model. Age–luminosity relations predict that the T_{int} of GJ 3090 b may be lower than 100 K (see Section 6.5); however, a higher temperature combined with vertical mixing can serve to quench CH₄, perhaps contributing to the observed muted features in GJ 3090 b’s spectrum. We allow a conservatively high T_{int} for this reason. The full posterior distributions for the equilibrium and disequilibrium grid-based retrievals are shared on Zenodo.

6. Results and Discussion

6.1. Impact of Stellar Activity on the NIRISS Observations

GJ 3090 is a relatively active M dwarf that affects both the light-curve analysis as well as the retrieved transmission spectra. Particularly for the NIRSpec transits, flares and spots produced correlated noise structures in our light curves, resulting in our choice to cut integrations for which we did not manage to find an adequate fit with any of our models (see Appendices B and E), though we note that our explorations into fitting models to the observed stellar flux variations did not show any effect on the resulting transmission spectrum (see Appendix B).

On the other hand, the observations in the bluer wavelength range with NIRISS/SOSS showed features that are well explained by stellar heterogeneities, burying any features and inferences about GJ 3090 b’s atmosphere (see Appendix C.2). Both visits demonstrated different inferred heterogeneity parameters irrespective of the retrieval code used (Figure 7;

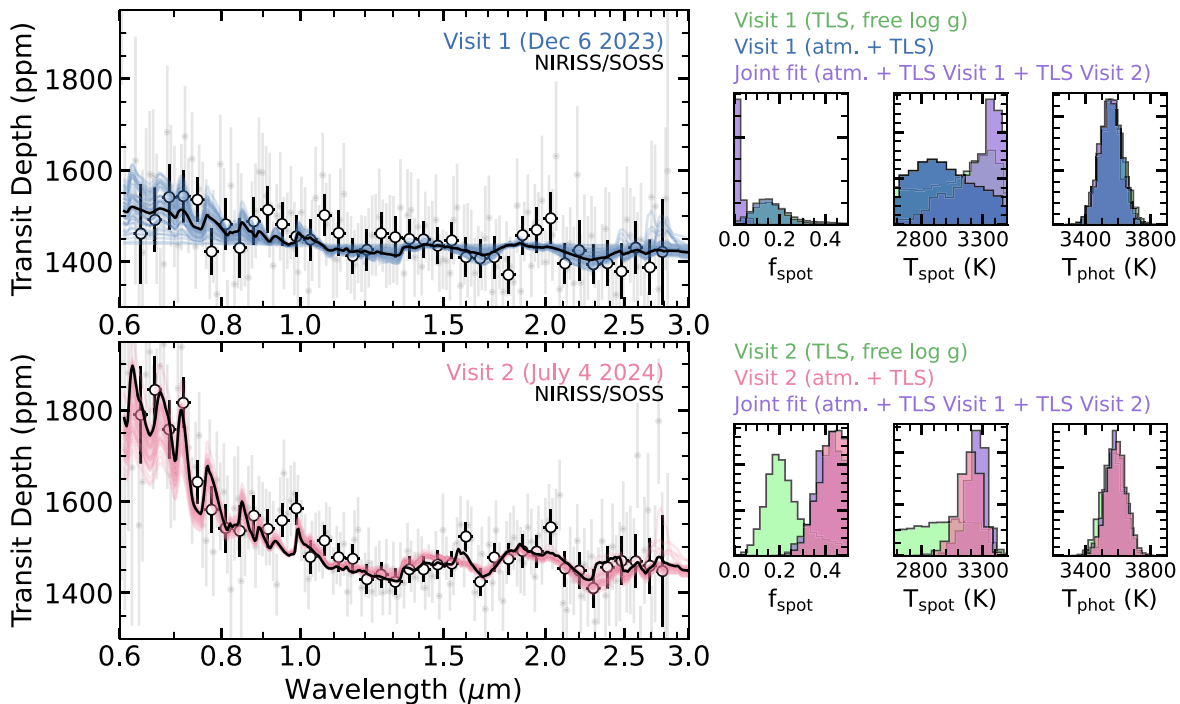


Figure 7. Results from the `stctm` stellar contamination retrievals and `SCARLET` joint retrieval of the atmosphere and stellar contamination components for retrievals performed on individual or both NIRISS/SOSS spectra of GJ 3090 b. Left panels: measured transmission spectrum (black data points) for the first (top panel) and the second (bottom panel) NIRISS/SOSS transits, along with the best-fitting model (black line) and sample spectra from the posterior distribution (semitransparent colored lines) from the individual atmosphere + TLS retrievals. We performed the retrievals on the $R = 100$ `exoTEDRF` spectra (gray points), also shown binned by a factor of 4 (black points) on the figure for visualization purposes. For the visit 1 (2) spectrum, the best-fit order 2 offset of -14.4 ($+94.4$) ppm was applied on the data points displayed. Right panels: marginalized posterior distributions on the stellar heterogeneity properties for the first (top) and second NIRISS/SOSS (bottom) visits. We show the results from `SCARLET` retrievals performed on individual visits (visit 1 in blue, visit 2 in pink) and on both visits assuming a shared atmosphere component but different stellar heterogeneity components (in purple). We also display the posterior distributions from the `stctm` retrievals to individual visits (green), which only accounts for the impact of the TLS effect on the observations (see Appendix C.2). The inferred heterogeneity properties are different for each visit, as evidenced by the difference in the blueward slope observed in the transmission spectrum. For visit 1, where stellar contamination is not confidently detected (see text), the joint fit to both visits only provides an upper limit on the spot covering fraction and a lower limit on the spot temperature.

Table 3), highlighting the stochasticity of appearing/disappearing spots on the surface within the time between the two SOSS visits (6 months/10 stellar rotation periods).

We also cross-check the stellar contamination retrieval results by performing fits directly to the out-of-transit NIRISS stellar spectra for both visits (e.g., H. R. Wakeford et al. 2019; S. E. Moran et al. 2023; M. Radica et al. 2025), and the heterogeneity parameters we infer from the out-of-transit analysis largely agree with those retrieved from the in-transit fits. More information on these fits can be found in Appendix C.1, and the results are summarized in Figure C1.

In what follows, we quote results from the `SCARLET` retrievals, since `SCARLET` supports the joint fitting of a planetary atmosphere to two NIRISS visits while accounting for visit-specific stellar contamination components, though we note that our conclusions from individual visit fits, in terms of the visit-to-visit changes in the stellar contamination component, are consistent across all three retrieval frameworks (Table 3). The results from the `SCARLET` retrievals including stellar contamination retrievals are shown in Figure 7. We find strong (5.07σ) evidence for stellar contamination shaping the spectrum for the second visit. The evidence for the presence of spots is even stronger (6.4σ) if hazes are not included in the atmosphere model. The inference of spots is also supported by the large inferred spot covering fractions, even when trying to explain both visits with the same atmosphere model, as well as the strong temperature contrast between the spots and the photosphere (see Figure 7). The model with spots favors an

offset of $69.87^{+31.19}_{-32.48}$ ppm between order 1 and order 2 (Table 3), but spots are detected regardless of whether an offset is included in the retrieval. We find no evidence for faculae from a Bayesian model comparison standpoint.

The conclusions for the first visit are more nuanced, which is expected given the less-pronounced short-wavelength slope (Figure 7). When a haze slope is included in our atmosphere model, we do not significantly detect spots in the visit 1 spectrum. In the absence of a Rayleigh slope enhancement from small-particle hazes, spots are detected at 2.1σ . The inferred spot properties are also less constrained than for the second visit, with large uncertainties on the spot temperature (Figure 7), and we only obtain an upper limit on the spot covering fraction (and a lower limit on the spot temperature) when the retrieval is performed under the assumption of a shared atmosphere component across both visits. Contrary to visit 2, even when fitting for an offset between order 1 and order 2 in the visit 1 spectrum, we do not retrieve a value different from 0 at the 1σ level.

When performing retrievals with a shared atmosphere and a TLS component that is either shared or visit-specific, the `SCARLET` retrievals have a slight (2.0σ) preference for visit-specific rather than shared stellar heterogeneity properties, which further highlights the time-variable nature of stellar heterogeneities. Finally, we find that consistent heterogeneity parameters can explain the spectrum in stellar-contamination-only retrievals (that is, if we assume that there is no contribution from GJ 3090 b’s atmosphere to the transmission

Table 5
Constraints on the Atmospheric Properties for the Retrievals on Each NIRISS/SOSS Visit

Parameter	SCARLET		Aurora		POSEIDON	
	Visit 1	Visit 2	Visit 1	Visit 2	Visit 1	Visit 2
Atmosphere Composition						
$\log_{10} \text{H}_2\text{O}$	<-0.67	<-1.05	N/A	<-2.97	<-1.26	<-2.08
$\log_{10} \text{CO}_2$	N/A	N/A	N/A	<-1.33	<-0.93	N/A
$\log_{10} \text{CH}_4$	<-1.14	<-1.14	<-1.62	<-4.25	<-2.06	<-2.76
$\log_{10} \text{SO}_2$	N/A	N/A	N/A	<-1.07	<-1.04	N/A
$\log_{10} \text{CO}$	N/A	N/A	<-0.96	N/A
$\log_{10} \text{H}_2\text{S}$	N/A	N/A	<-1.23	N/A
$\log_{10} \text{HCN}$	<-1.02	<-1.14
$\log_{10} \text{NH}_3$	<-1.7	<-2.64
Temperature						
T_{atm} (K)	<895.45	<892.93	<332.7	<351.53	<489.58	<542.93
Clouds and Hazes						
$\log_{10} \rho_{\text{cloud}}$ (bars)	<-2.54	<0.66	$-3.08^{+2.91}_{-3.14}$	$-2.03^{+2.46}_{-3.62}$	$-2.7^{+2.45}_{-2.17}$	$-1.92^{+2.12}_{-2.35}$
f_{cloud} (%)	66^{+20}_{-29}	57^{+24}_{-27}
$\log_{10} a$	>-2.61	>-2.21	$4.35^{+1.98}_{-3.8}$	$1.67^{+3.16}_{-3.11}$
γ	$-7.46^{+4.15}_{-6.05}$	<-0.95	$-5.55^{+3.01}_{-6.24}$	$-9.96^{+5.86}_{-5.78}$
Reference Pressure or Radius						
p_{ref} (bar)	... ^a	... ^a	$-3.8^{+3.14}_{-2.84}$	$-3.07^{+2.7}_{-3.09}$
R_{ref} (R_{\oplus})	$2.06^{+0.06}_{-0.05}$	$2.01^{+0.07}_{-0.05}$	$1.95^{+0.06}_{-0.1}$	$2.0^{+0.03}_{-0.08}$

Note. Performed with SCARLET (model with uniform clouds and no hazes), Aurora (model including hazes and patchy clouds), and POSEIDON (model with hazes and uniform clouds). Since the spectrum is best explained by stellar contamination alone, several atmospheric parameters are unconstrained with a posterior consistent with the prior; in these cases, we simply report N/A for the constraints, while an ellipsis means that the parameter was not fitted in that retrieval configuration. Lower or upper limits are reported at 2σ .

^a In the SCARLET retrievals, p_{ref} is fitted at each step to find the best match to the observed spectrum but is not recorded.

spectra). However, lower spot covering fractions are allowed in visit 2 when the gravity of the stellar photosphere and the heterogeneity components are allowed to adopt values larger than the literature value—something preferred both in the `stctm` fit and in the fit to the out-of-transit stellar spectra. We additionally perform tests using POSEIDON where we use two nested models to explain each NIRISS visit: one including only colder stellar heterogeneities (spots) and another where both spots and a minimal planetary atmosphere are considered (as defined in the POSEIDON section of Section 5.2.1). We find that heterogeneity parameters consistent with those of the SCARLET joint retrieval are inferred in each scenario, and that the addition of the atmospheric component is not required from a Bayes factor standpoint (favored by $<2\sigma$ for both of the visits). This highlights the fact that no meaningful atmospheric constraints can be placed from our joint TLS–atmosphere retrievals on the NIRISS spectra (Table 5).

Finally, while stellar contamination can also impact transmission spectra at longer wavelengths (although to a lesser extent), we find that it does not affect the main conclusions we draw on the atmospheric inferences (Figure D1). Our constraints on SO_2 and CH_4 remain largely unchanged when considering an additional spot component in our model, while our constraints on the water abundance become less meaningful (since the star can produce “fake” water features), with a broad posterior compared to the lower limits from atmosphere-only fits. Our inference of high metallicity is not impacted, however, as the retrieval compensates overall lower water abundances with higher CO_2 abundances to retain a high atmospheric MMW, similar to that inferred from atmosphere-only modeling (Figure D1).

We recommend for future observation planning that NIRISS and NIRSpec observations be scheduled close in time such that a consistent TLS model can reasonably be assumed to hold for both instruments, which can thereby help break the atmosphere–TLS degeneracy present in spectra from both instruments. A similar experimental design was tested for LHS 1140 b by C. Cadieux et al. (2024), who observed two consecutive transits separated by 24.7 days with NIRISS. The two spectra showed consistent TLS configurations over this time period, which represents $\sim 20\%$ of the stellar rotation period (C. Cadieux et al. 2024). In our case, though, stellar contamination broadly prevents us from placing meaningful constraints on the planetary atmosphere from the NIRISS observations alone (with broad unconstrained molecular abundance posteriors).

6.2. The Atmospheric Composition of GJ 3090 b

We use three types of retrievals and models to interpret the NIRSpec/G395H spectrum of GJ 3090 b in terms of its atmospheric composition: (1) free retrievals with SCARLET, POSEIDON, and Aurora; (2) chemical equilibrium retrievals with SCARLET; and (3) forward models using the `ScCHIMERA` “grid-based retrieval” approach and chemical disequilibrium forward model calculations using `ScCHIMERA` paired with `VULCAN`. The free retrieval approach is the most agnostic, as it makes no assumption about the atmospheric chemistry and instead infers atmospheric abundances independently from each other, from the observed spectrum. Still, for sub-Neptunes with muted spectral features, chemical equilibrium models have proved useful to assess the range of atmospheric scenarios compatible with the data (see, e.g., N. L. Wallack et al. 2024;

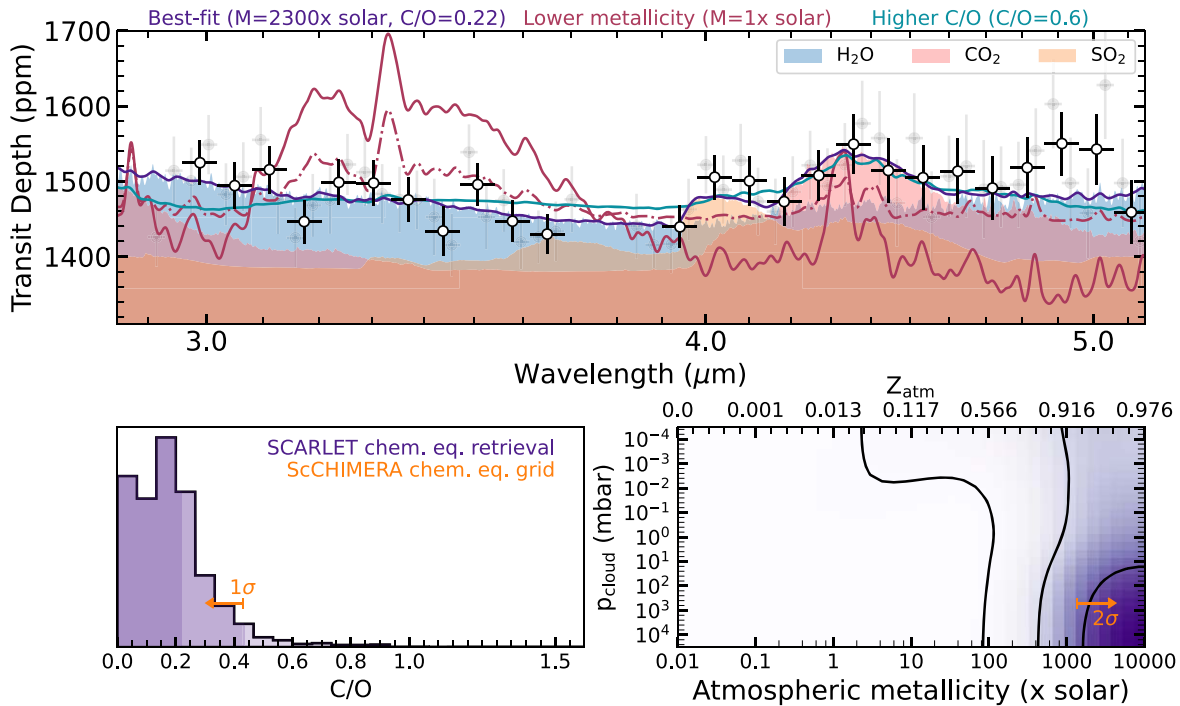


Figure 8. The confident nondetection of CH_4 at $\sim 3.4 \mu\text{m}$ in the NIRSPEC/G395H spectrum drives our inference of a high-metallicity atmosphere, while the tentative SO_2 feature suggests a low-C/O atmosphere on GJ 3090 b. Top panel: NIRSPEC/G395H visit 1+2 transmission spectrum from exoTEDRF (gray points, used for retrieval) and the binned spectrum (black points), with representative atmosphere models. The purple line is the best-fitting chemically consistent model, while the pink model highlights the impact of lowering the metallicity to $1\times$ solar (solid line: cloud-free model; dashed-dotted model: clouds at 1 mbar), and the blue model illustrates the expectation for a higher-C/O ($\text{C}/\text{O} = 0.6$) atmosphere. For the low-metallicity case, CH_4 , rather than H_2O absorption, dominates over the wavelength range covered by the NRS1 detector. The color shadings illustrate the contributions of H_2O , CO_2 , and SO_2 to the model spectrum. Bottom panels: posterior distributions on the atmospheric C/O ratio and metallicity from the SCARLET chemical equilibrium retrieval (purple) as well as the ScCHIMERA equilibrium grid fits (1σ upper limit on the C/O ratio and 2σ lower limit on the metallicity quoted in orange). The left panel is the C/O ratio, with the 1σ , 2σ , and 3σ upper limits shown in different color shadings. The right panel is the joint posterior distribution on the atmospheric metallicity and cloud-top pressure (1σ , 2σ , and 3σ contours for the SCARLET retrievals outlined in black), which highlights that the small-amplitude features in our spectrum favor a high-metallicity atmosphere on GJ 3090 b.

J. Teske et al. 2025). We recognize, however, that the atmosphere of GJ 3090 b may not be in chemical equilibrium, as seen for TOI-270 d (B. Benneke et al. 2024), and use disequilibrium models to assess the impact of the chemical equilibrium assumption on our findings.

Our free retrievals find no evidence for CH_4 in the atmosphere of GJ 3090 b (Figure D1), despite our sensitivity to the prominent CH_4 band near $3.3 \mu\text{m}$. We also find that an abundance of heavy molecular species (H_2O , CO_2 , or SO_2) is preferred as an explanation for the muted spectral features, even when stellar contamination is jointly fitted with atmospheric properties (Table 4, Figure D1). The SCARLET, POSEIDON, and Aurora retrievals consistently yield lower limits on the abundances of H_2O and CO_2 , two-sided (broad) constraints on the SO_2 abundance (VMR $-4.83^{+1.16}_{-2.54}$ from SCARLET, $-4.34^{+1.65}_{-3.28}$ from POSEIDON, and $-5.37^{+1.61}_{-2.94}$ from Aurora), and a 2σ upper limit of ~ 100 ppm on the CH_4 abundance (Figure D1). Although H_2O , CO_2 , and SO_2 are not individually significantly detected from a model comparison standpoint, the model requires the presence of at least one of these heavy molecules at 3.4σ (significance from the SCARLET retrieval). The low signal-to-noise of the atmospheric signatures does not enable us to infer the atmospheric metallicity from free retrievals, and obtaining a directly data-driven metallicity constraint from this chemistry-agnostic approach would require repeat observations.

As noted in the previous subsection, our conclusion of a high metallicity from the NIRSPEC transmission spectrum is robust to the consideration of stellar contamination, as it cannot falsely

cause a detection of SO_2 or CO_2 . Indeed, we verify with an additional POSEIDON retrieval, identical to the free chemistry retrievals described above but with the addition of the effects of TLS, that when we include TLS in our NIRSPEC retrievals, the abundance of H_2O is unconstrained; however, the high abundances of CO_2 and SO_2 , as well as the nondetection of CH_4 , remain.

The results from the chemically consistent retrievals are shown in Figure 8. Despite having fewer parameters and making the assumption that all molecular abundances follow chemical equilibrium expectations (except for SO_2 when it is fitted independently), the SCARLET retrievals enable us to start drawing more meaningful conclusions about the atmospheric chemistry than the free retrievals, since we obtain limited information on individual molecular abundances due to the highly muted features in the spectrum of GJ 3090 b. However, even if the spectral features have low amplitudes, they are significant enough to enable us to rule out clouds as the origin of their low amplitudes, at least in the most metal-poor atmospheres (at the 3σ level, our observations could still be explained by clouds at pressures of less than $10 \mu\text{bar}$ in a $10\times$ solar metallicity atmosphere; Figure 8). The preference for high-metallicity and generally subsolar C/O ratios as the explanation for the transmission spectrum is independently supported by the ScCHIMERA chemical equilibrium grid-based retrieval results that incorporate an additional level of consistency with pressure-temperature profiles calculated self-consistently in chemical equilibrium rather than prescribed by the observations (as in the SCARLET retrievals). The C/O is

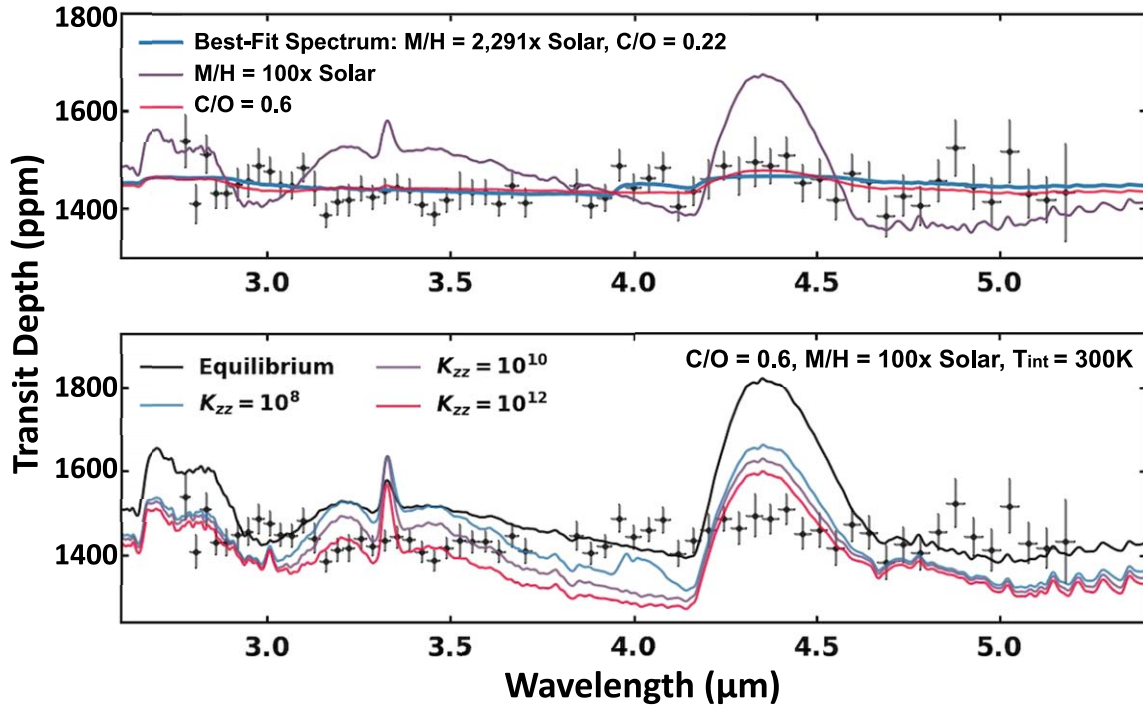


Figure 9. The effects of varying the atmosphere chemistry on the NIRSpec/G395H transmission spectrum of GJ 3090 b. Top: plotted in blue is the best-fit spectrum from the grid-based 1D-RCTE retrieval with `SCCHIMERA`. In purple and red are model spectra with the same parameters as the best-fit model but with M/H set to $100\times$ solar or C/O set to 0.6, respectively. Bottom: models with adjusted K_{zz} , demonstrating that even a large degree of vertical mixing combined with a high internal temperature (in this case, plotted models assume $T_{\text{int}} = 300$ K, while our grid-based retrievals assume a lower $T_{\text{int}} = 100$ K) cannot sufficiently deplete CH_4 even in a lower-metallicity atmosphere ($C/O = 0.6$, $M/H = 100\times$ solar) to match the lack of observed spectral features.

similarly unconstrained in the grid-based chemical equilibrium retrievals, although subsolar values are preferred (Figure E3). In agreement with the chemically consistent retrieval findings, the lack of constraints on cloud parameters (κ_{cloud} and a cloud covering fraction) demonstrates that clouds cannot sufficiently mute spectral features to explain the observed NIRSpec/G395H spectrum without invoking high metallicity.

Overall, the inference of high metal enrichment from chemical equilibrium modeling is driven by the muted spectral features in the infrared (Figure 8), with a potential spectroscopic signature of CO_2 at $\sim 4.2 \mu\text{m}$ and the lack of CH_4 . Note that the absence of the methane feature is not necessarily an indicator of high metallicity in exoplanet atmospheres, as it can be achieved even in low-metallicity atmospheres provided that methane is depleted by disequilibrium chemistry, such as photochemistry, or quenching due to interactions with a hot interior (e.g., J. J. Fortney et al. 2020). We examine the impact of disequilibrium chemistry using the `SCCHIMERA` self-consistent forward-modeling approach. Even when considering a high interior temperature of 300 K (which may be allowable due to tidal heating from a nonzero orbital eccentricity; see Section 6.5) and strong mixing with a C/O of 0.6 (relatively high compared to what was found by the retrievals; see Figure 8), we find that quenching in a low-metallicity atmosphere cannot reproduce the level of methane depletion we observe (Figure 9). This modeling demonstrates the robustness of the high-metallicity conclusion in the self-consistent modeling approach, even in the presence of quenching driven by a hot interior. This high metallicity would not be representative of an H_2 -rich envelope. Meanwhile, the low- C/O conclusion requires further investigation as it hinges

more strongly on the presence of SO_2 , for which we do not achieve a significant detection.

Finally, we once again use `POSEIDON` to compare the data-model fit statistics from our NIRSpec/G395H retrievals to a flat-line fit using the minimal atmosphere models outlined in the `POSEIDON` section of Section 5.2.1. Our nested Bayesian model comparison results in a $\sim 2.1\sigma$ preference for our minimal atmosphere-only model to a flat line, demonstrating moderate evidence for the presence of atmospheric features. Similarly, we find a $\sim 2.1\sigma$ preference for our joint minimal atmosphere-TLS model over our spots-only model, suggesting that our atmospheric signal cannot merely be attributed to stellar contamination. This indicates that the presence of both an atmosphere and stellar spots best explains the observed NIRSpec/G395H spectrum.

6.3. Helium Absorption Supports a Metal-enriched Atmosphere

We find strong evidence for helium absorption in the transmission spectrum of GJ 3090 b, though the resolution of NIRISS/SOSS is not high enough to constrain the width and shape of the helium triplet absorption and as such is not sufficient to provide constraints on the hydrodynamic escape of GJ 3090 b's atmosphere. This follows the prediction by L. A. Dos Santos et al. (2023) and has also been borne out in the analysis of the NIRISS/SOSS observations of the warm Jupiter HAT-P-18 b (G. Fu et al. 2023; M. Fournier-Tondreau et al. 2024).

We model the predicted excess metastable helium absorption for GJ 3090 b using the `p-winds` (L. A. Dos Santos et al. 2022) python wrapper for the 1D photoionization hydrodynamic code `ATES` (A. Caldiroli et al. 2021; F. Biassoni et al.

2024). ATES assumes a nonisothermal atmosphere, allowing us to self-consistently calculate the temperature profile as a function of radial distance by obtaining solutions that do not violate energy conservation (A. Caldiroli et al. 2021). Using ATES, the planet parameters, and a proxy stellar spectrum of GJ 832 from the MUSCLES survey (A. Youngblood et al. 2016) that matches GJ 3090 closely in terms of stellar parameters (T_{eff} , $\log g$, $\log R'_{\text{HK}}$), we calculate the predicted metastable helium absorption and mass-loss rate for GJ 3090 b assuming a 90/10 H_2/He ratio. We find a predicted excess absorption of $\sim 3.5\%$ at the metastable helium wavelengths, consistent with the strong absorption signals predicted for planets orbiting M-type hosts (F. Biassoni et al. 2024). However, convolving our signal with the resolution of NIRISS/SOSS at the metastable helium wavelengths, we find a predicted excess absorption for GJ 3090 b with NIRISS/SOSS of 0.51%, corresponding to a mass-loss rate of $\log \dot{M}$ of 10.1 (cgs). If assumed to be constant in time, this would yield an upper limit of ~ 50 Gyr for photoevaporation to completely strip the planet of its atmosphere.

However, it is critical to note that this modeled absorption is a factor of 10 higher than we have detected in our observations (434 ± 79 ppm or $0.0434\% \pm 0.0079\%$). The models used to predict the excess absorption and mass-loss rate are optimized for solar metallicity atmospheres (A. Caldiroli et al. 2021; F. Biassoni et al. 2024). While most mass-loss models do not have metallicity as a tunable parameter, previous works (e.g., J. E. Owen & A. P. Jackson 2012; J. E. Owen & R. Murray-Clay 2018; M. Zhang et al. 2022a, 2025; S. Vissapragada et al. 2024b) have shown that as metallicity increases, particularly beyond $\sim 100\times$ solar, the excess absorption signal and mass-loss rate are significantly reduced. This, therefore, provides an independent line of evidence that the metallicity of GJ 3090 b's atmosphere is indeed highly elevated, and the envelope lifetime derived above should be taken as a lower limit, as a decreased mass-loss rate due to elevated atmosphere metallicity will increase the atmospheric lifetime.

A potential caveat to this conclusion is that the comparative weakness of the He signal that we detect could be due to He depletion, as has been inferred for Jupiter (e.g., U. von Zahn et al. 1998) as well as WASP-80 b (e.g., L. Fossati et al. 2023). However, sub-Neptunes at the upper edge of the radius valley are instead predicted to potentially be He-enriched (e.g., I. Malsky et al. 2022; C. Cherubim et al. 2024, 2025), making the He-depletion scenario less plausible a priori.

Further observations with high-resolution instruments will allow us to resolve the metastable helium line, providing better constraints on the mass-loss rate, outflow temperature, and velocity structure of the outflow. This marks another sub-Neptune helium detection that is lower than expected, consistent with ground-based observations (M. Zhang et al. 2022a, 2022b), though the first using JWST.

6.4. Potential Scenarios Leading to Metal Enrichment

There are multiple pathways through which sub-Neptunes can become metal-enriched. Formation theories propose that these planets may acquire their metal enrichment by accreting metal-rich planetesimals (e.g., J. J. Fortney et al. 2013). A large amount of solids in the form of water ice could have been accreted onto GJ 3090 b's atmosphere if it formed beyond the ice line (A. Léger et al. 2004; R. Luger et al. 2015; Y. Alibert & W. Benz 2017; E. S. Kite & E. B. Ford 2018; J. Venturini et al.

2020; B. Bitsch et al. 2021). With planet migration mechanisms, the planet could have later moved closer to its host star and become warm enough that a fraction of the accreted material sublimates and ends up as water vapor in the atmosphere, increasing the metallicity. Alternatively, volatiles could even sublimate directly upon their initial accretion into the growing atmosphere.

For warm and hot sub-Neptunes, however, it is also expected that their envelopes experience significant mass loss due to hydrodynamic atmospheric escape processes (J. E. Owen & Y. Wu 2017; S. Ginzburg et al. 2018), which can create a high-metallicity atmosphere. Hydrodynamic escape can be powered by the high X-ray and ultraviolet irradiation from the host star (photoevaporation; e.g., A. J. Watson et al. 1981; H. Lammer et al. 2003; A. Vidal-Madjar et al. 2003; N. V. Erkaev et al. 2007; D. Ehrenreich et al. 2015; M. Salz et al. 2016) and/or a planet's internal energy from formation (core-powered mass loss; e.g., S. Ginzburg et al. 2018; A. Gupta & H. E. Schlichting 2019, 2020). Given the ~ 1 Gyr age of GJ 3090 (J. M. Almenara et al. 2022) and the observed helium escape (see Section 4), one plausible explanation for its observed metal-rich atmosphere could be the extensive history of hydrodynamic atmospheric escape that has progressively removed a H_2/He envelope.

Recent works by I. Malsky et al. (2022), C. Cherubim et al. (2024), and Louca et al. (submitted) underscore the transformative role of hydrodynamic escape on the atmospheric evolution for sub-Neptune and Neptune-sized exoplanets. For example, the findings from Louca et al. indicate that extreme hydrodynamic escape can significantly enrich atmosphere metal content for planets with equilibrium temperatures between 700 and 1000 K, resulting in a water-enriched atmosphere after ~ 300 Myr. They also showed a notable decrease in the atmospheric C/O ratio due to the drag of heavier elements.

Another possible scenario is to enrich the atmosphere by interactions between a magma ocean and the atmosphere, producing significant amounts of molecules such as H_2O in the H_2/He -rich envelopes directly above the magma ocean (e.g., E. S. Kite & L. Schaefer 2021; H. E. Schlichting & E. D. Young 2022; T. Lichtenberg & Y. Miguel 2024; J. G. Rogers et al. 2024). While we would expect H_2O features in GJ 3090 b's atmosphere, we are not able to robustly constrain the water abundance in the atmosphere of GJ 3090 b due to degeneracies with stellar contamination. So we cannot make any statements about the hydrogen budget in the atmosphere at this point in time. Nevertheless, this mechanism suggests that oxidized planets enrich the atmosphere with O-rich species, also including CO_2 or SO_x compounds, in line with our potential findings of these species in the spectrum of GJ 3090 b.

6.5. Potential Implications for the Interior

The interior structure of sub-Neptunes is highly degenerate between the composition and mass of the core and the amount of H/He in the envelope (J. J. Fortney et al. 2013; J. F. Otegi et al. 2020), and to resolve this degeneracy, atmospheric characterization data are crucial. Here we estimate conclusions on the mass of the core of GJ 3090 b we can draw when we assume the metal mass fraction of the envelope (Z_{env}) to be constrained by the one derived from our atmospheric modeling analysis (see Figure 8, bottom right panel).

We generate a suite of interior structure models with the GAS giant model for Interiors (GASTLI; L. Acuña et al. 2021, 2024). GASTLI models the planetary interior as two layers: a metal-rich core and an envelope. The core, which in this work we refer to as the mass of the region where metals are found outside the envelope, comprises rocks and water in a 1:1 mass ratio, while the envelope consists of H/He and water. A 1:1 water-to-rock ratio for the core has previously been assumed in interior models of gas giants and sub-Neptunes (J. J. Fortney et al. 2007). The exact core compositions of volatile-rich planets remain uncertain, even for the solar system gas and ice giants, despite the availability of Love numbers and gravitational field data (R. Helled & S. Howard 2024). Furthermore, sub-Neptunes can exhibit a wide range of ice-to-rock ratios depending on their formation locations (O. Mousis et al. 2019; J. Mah et al. 2024). Thus, the 1:1 water-to-rock core composition provides a simple and reasonable starting assumption. The metal mass fraction of the envelope, Z_{env} , and the core mass fraction (CMF) are user-defined parameters. In this work, we use the publicly available atmospheric grid from E. M. R. Kempton et al. (2023, hereafter K23) to calculate the interior-atmosphere boundary temperature at 1000 bars. This grid is suitable for GJ 3090 b given its equilibrium temperature, low surface gravity, and M dwarf host star. K23 adopt water as the only metal absorber in their opacity calculations, rather than scaling absorbers such as CH_4 , CO , and CO_2 according to solar abundances. To assess opacity-driven differences, we compared pressure-temperature profiles from K23 and GASTLI’s default atmospheric grid, which includes a solar-scaled mix of absorbers (P. Mollière et al. 2015; L. Acuña et al. 2024). Using the same set of equilibrium and internal temperatures and surface gravity consistent with GJ 3090 b, K23’s grid predicts a temperature 250 K warmer at 1000 bars than the `petitCODE` grid. L. Acuña et al. (2023) report that such temperature differences (200 K) result in radius variations of 1% for sub-Neptunes, well below the 5% observational uncertainty in GJ 3090 b’s radius.

In addition to the CMF and envelope metal mass fraction, the intrinsic (or internal) temperature can strongly influence the planet’s radius, particularly for younger planets (E. D. Lopez & J. J. Fortney 2014). The age of GJ 3090 is $1.02^{+0.23}_{-0.15}$ Gyr (J. M. Almenara et al. 2022). We estimate the internal temperature of GJ 3090 b by comparing its radius and age (including uncertainties) with thermal evolution curves calculated at different CMFs and Z_{env} at a constant mass of $M_p = 3.34 M_{\oplus}$ with GASTLI. We set a lower bound of $Z_{\text{env}} = 0.90$, as the 3σ limit of the envelope metal mass fraction from atmospheric retrievals is ~ 0.916 . This analysis constrains GJ 3090 b’s internal temperature to $T_{\text{int}} = 20\text{--}40$ K and $20\text{--}70$ K within 1σ and 3σ , respectively. Within the $20\text{--}70$ K range, the planet radius increases by $0.05 R_{\oplus}$, which is below the observational radius uncertainty, $\sigma(R) = 0.11 R_{\oplus}$. Therefore, we adopt a nominal value of $T_{\text{int}} = 40$ K for the computation of mass-radius curves.

Figure 10 presents the mass-radius curves for GJ 3090 b, assuming $T_{\text{eq}} = 693$ K, $T_{\text{int}} = 40$ K, and envelope metal mass fractions ranging from $Z_{\text{env}} = 1$ (pure water) to 0.90. The mass and radius of GJ 3090 b are compatible with a CMF of $\sim 0.99\text{--}0.50$ for a pure water envelope ($Z_{\text{env}} = 1$) at the 1σ level. For envelopes containing H/He, a CMF of 0.60 remains consistent with the mass and the radius at the 3σ level. Thus, we can conclude that if GJ 3090 b has a well-mixed core of

rock and ice (i.e., water in supercritical and/or superionic phases; see J. Haldemann et al. 2020; O. Mousis et al. 2020), its mass fraction lies between 0.50 and ~ 1 .

Sub-Neptunes that form close to the water-ice line may accrete ice-rich material, resulting in cores where ice and rock are miscible (A. Vazan et al. 2022; H. Luo et al. 2024). In contrast, formation inside the ice line or close to the Fe and Si lines may produce dry cores dominated by silicates and Fe (E. J. Lee & E. Chiang 2016; A. Aguichine et al. 2020). To explore this scenario, we include mass-radius curves for pure rock and Earth-like cores (A. Aguichine et al. 2021), which correspond to no Fe and 32% Fe by mass, respectively. In these models, the envelope is entirely constituted by water. Figure 10 shows that GJ 3090 b’s mass and radius are consistent with CMFs = 0.50–0.70 (1σ) for pure rock cores, while CMFs < 0.30 are ruled out at the 3σ level. For Earth-like cores, CMFs > 0.90 are inconsistent with the mass and radius data beyond 3σ .

7. Summary and Conclusions

In this Letter, we presented four transit observations of GJ 3090 b with JWST, two each with NIRISS/SOSS and NIRSpec/G395H as part of a JWST sub-Neptune survey (GO 4098; PIs: B. Benneke, T. Evans-Soma).

We detect absorption from the He I triplet at $1.0833 \mu\text{m}$ in the NIRISS/SOSS pixel-level transmission spectra in both independent reductions and both visits at a statistical significance of $> 5\sigma$. The observed amplitude is an order of magnitude smaller than predicted by forward models with solar metallicity, independently supporting the inferred high metallicity for GJ 3090 b’s atmosphere. We also predict that this absorption feature is observable with ground-based high-resolution spectrographs that can further constrain the mass loss and outflow temperature.

We detect strong ($\sim 5\sigma$) evidence for the TLS effect in the NIRISS/SOSS wavelength range, preventing any robust constraints on the planetary atmosphere. We find that the two SOSS visits, taken 6 months (~ 10 stellar rotation periods) apart, showed a difference in stellar heterogeneity parameters, highlighting the variable nature of the stellar contamination signals. This prohibited any atmospheric inferences from the NIRISS/SOSS data, as TLS-only retrieval models were preferred over TLS+atmosphere models.

Moreover, offsets between the NIRISS and NIRSpec spectra and between the two NIRISS visits, which could not be traced back to data reduction or light-curve fitting differences, also suggest different stellar contamination realizations between spectra from the two instruments. These variable impacts of the TLS effect all but precluded joint atmosphere analyses of the NIRISS and NIRSpec spectra. Therefore, we recommend that future exoplanet observations that need both NIRISS and NIRSpec for their science are scheduled close enough in time that the star’s photosphere will not have significantly changed and a single TLS realization can be assumed for spectra from both instruments.

Using the two NIRSpec/G395H visits, we presented atmospheric retrievals in addition to chemically consistent retrievals and a grid analysis to explore the impact of disequilibrium chemistry. We find that GJ 3090 b’s spectrum is best explained by a high-metallicity atmosphere. The best-fitting grid models prefer a $> 1000\times$ solar metallicity atmosphere (best fit at MMW ~ 27 amu), and chemically consistent retrievals indicate

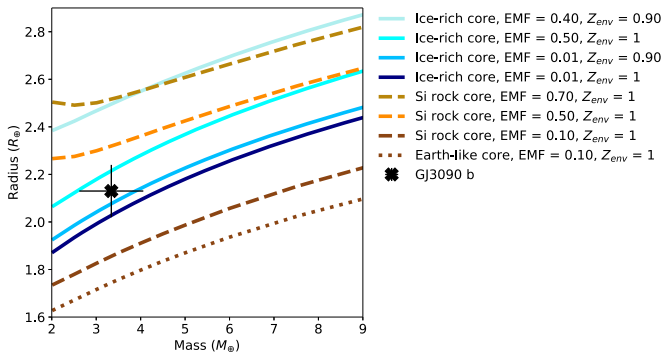


Figure 10. Mass–radius curves for GJ 3090 b ($T_{\text{eq}} = 693$ K) at varying core compositions (ice-rich, pure silicate rock, and Earth-like iron-to-rock ratio), envelope mass fractions (EMFs), and mass fractions of metals in the envelope (Z_{env}). The GASTLI models (solid lines) assume a miscible 1:1 ice and rock core, whereas the A. Aguichine et al. (2021) models (dashed and dotted lines) assume dry, pure rock (no Fe) and Earth-like (32% Fe) core compositions.

a metallicity $>100\times$ at 3σ confidence for clouds at $<\mu\text{bar}$ pressures, or $>700\times$ solar at 2σ irrespective of the presence of clouds. The free retrievals were not able to constrain any one molecule, though the presence of at least one high-MMW molecule is favored by 3.4σ . Both the high metallicity and the subsolar C/O ratio could be explained by ice-rich formation or atmospheric evolution under chemical exchange with the interior and/or atmospheric mass loss.

However, our findings are subject to certain caveats. First, while we conducted a comprehensive analysis regarding stellar contamination and the systematics in our data, we note that any underestimation (or overestimation) of the TLS effect or inaccuracies in the stellar models can affect our retrieved atmospheric constraints. In addition, due to the almost featureless nature of the transmission spectrum of GJ 3090 b in the NIRSpec wavelength range and the stellar contamination in NIRISS, our retrieved atmospheric constraints may be biased based on model assumptions. The chemically consistent modeling may be limited, while the free chemistry may be hindered by its flexibility. The chemically consistent models are largely informed by the muted features and potential hints of heavier molecules, like CO_2 and SO_2 , in the atmosphere. However, the lack of CH_4 could also be explained by chemistry we do not consider in our modeling, e.g., associated with 3D effects as have been explored for hot Jupiters (M. Zamyatina et al. 2023, 2024). On the other hand, free chemistry retrievals favor at least one of the heavy molecules to be present in GJ 3090 b’s atmosphere at 3.4σ . Therefore, both our chemically consistent and free chemistry modeling suggest a high-metallicity atmosphere that is in line with what was found in recent CRIRES+ observations (L. T. Parker et al. 2025), though further observations are needed to definitively detect absorption from carbon- and sulfur-bearing species in the atmosphere of GJ 3090 b.

Acknowledgments

This work is based on observations with the NASA/ESA/CSA James Webb Space Telescope, obtained at the Space Telescope Science Institute (STScI) operated by AURA, Inc. All of the data presented in this Letter were obtained from the Mikulski Archive for Space Telescopes (MAST) at the Space Telescope Science Institute. The data used in this Letter can be found in MAST at the following DOI:10.17909/r2bz-wb41. E.

A. is grateful for the support from the Max Planck Gesellschaft (MPG) and the Deutsches Zentrum für Luft- und Raumfahrt (DLR). M.R. acknowledges support from the Natural Sciences and Engineering Research Council of Canada (NSERC) and the Fonds de recherche de Québec—nature et technologie (FRQNT). C.P.G. acknowledges support from the NSERC Vanier scholarship and the Trotter Family Foundation. C.P.G. also acknowledges support from the E. Margaret Burbidge Prize Postdoctoral Fellowship from the Brinson Foundation. H. E.S. gratefully acknowledges support from JWST grant #JWST-GO-04098.005-A. R.A. acknowledges the Swiss National Science Foundation (SNSF) support under the Post-Doc Mobility grant P500PT_222212 and the support of the Institut Trotter de Recherche sur les Exoplanètes (iREx).

Data Availability

Data products (light curves and transmission spectra) and modeling outputs (posterior distributions and best-fit models) are available on Zenodo at <https://doi.org/10.5281/zenodo.15273592>.

Facility: JWST (NIRSpec and NIRISS).

Software: astropy (Astropy Collaboration et al. 2013, 2018), batman (L. Kreidberg 2015), celerite (D. Foreman-Mackey et al. 2017), emcee (D. Foreman-Mackey et al. 2013), Eureka! (T. J. Bell et al. 2022), exoTEDRF (M. Radica 2024a), ExoTiC-LD (D. Grant & H. Wakeford 2024), exoUPRF (M. Radica 2024b), ipython (F. Pérez & B. E. Granger 2007), jwst (H. Bushouse et al. 2023), matplotlib (J. D. Hunter 2007), MCMC (D. Foreman-Mackey et al. 2013), numpy (C. R. Harris et al. 2020), scipy (P. Virtanen et al. 2020), Tiberius (J. Kirk et al. 2017, 2021; E. Ahrer et al. 2022).

Appendix A

Joint Light-curve Fitting: Constraints on Eccentricity

In their initial analysis of the GJ 3090 b system, J. M. Almenara et al. (2022) are not able to give firm constraints on the orbital eccentricity of GJ 3090 b, with Keplerian and “dynamical” modeling suggesting a nonzero eccentricity between 0.16 and 0.18, which relaxes to $e < 0.32$ at 3σ confidence when considering the long-term stability of the orbits of planets b and c. We therefore take an agnostic approach to the eccentricity in our fits, considering three separate cases: fixing $e = 0$, fixing $e = 0.15$ consistent with the dynamical and Keplerian modeling of J. M. Almenara et al. (2022), and leaving the eccentricity free. Figure A1 shows the impact of the eccentricity on the fitted orbital parameters (inclination and scaled semimajor axis). When fitting the transit white light curves of an individual visit, the eccentricity treatment does not have a significant impact on the other orbital parameters (S. Seager & G. Mallén-Ornelas 2003). However, there is a substantial impact when jointly fitting the four transits due to the eccentricity’s impact on the time of transit. In the joint fitting case, the fixed zero and nonzero eccentricity results bracket the free-eccentricity case, indicating that we do not have a significant constraint on the orbital eccentricity from this data set. The best-fitting eccentricity from the free-eccentricity joint fit is slightly nonzero (Table 2), though it is consistent with zero when considering the Lucy–Sweeney bias (L. B. Lucy & M. A. Sweeney 1971).

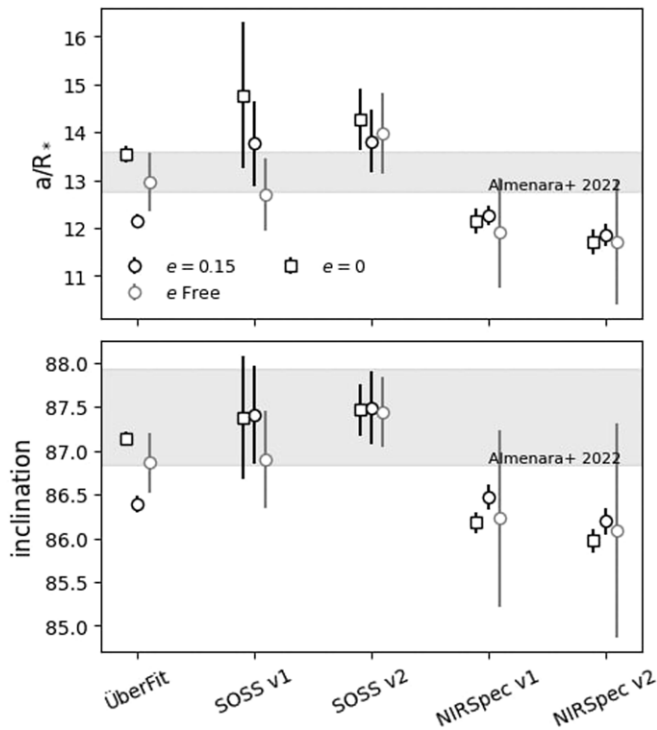


Figure A1. Comparison of derived orbital parameters using different data sets. The joint “überfit” uses all four observed transit white light curves, whereas the other four cases use the light curves from an individual visit. Three cases are shown for each fit: assuming a circular orbit, fixing the eccentricity to 0.15, and leaving the eccentricity free. The constraints from J. M. Almenara et al. (2022) are marked with gray shading. In general, NIRSpec prefers smaller values of a/R_* and inclination (which are positively correlated). The joint fit values are consistent with the findings of J. M. Almenara et al. (2022), except in the case where we fix $e = 0.15$.

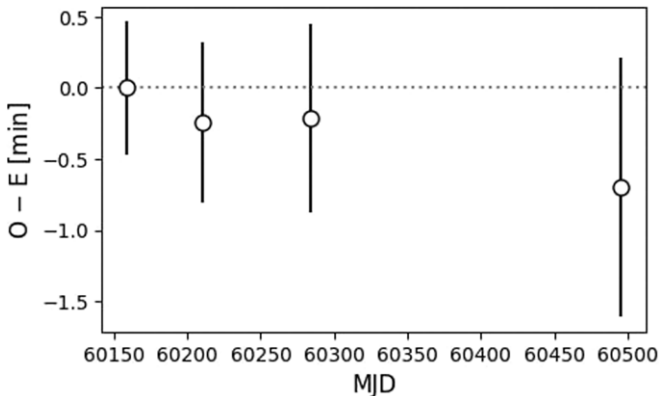


Figure A2. Midtransit times for each visit compared to a linear ephemeris propagated from visit 1. There is a slight trend to earlier times, with the final visit occurring approximately 1 minute earlier than would be expected from the linear ephemeris (though still consistent with zero with the propagated error), potentially suggesting some evidence for a nonzero orbital eccentricity or dynamical interactions with a potential planet c.

This is also demonstrated in Figure A2, where we show the times of midtransit obtained from fitting each visit separately and assuming a circular orbit compared to what would be expected given a circular orbit. Although all differences are consistent with zero within the propagated errors, there is a slight trend to earlier transit times, with the final visit occurring ~ 1 minute earlier than predicted. This potentially indicates

evidence of a nonzero eccentricity in GJ 3090 b’s orbit or dynamical interactions with planet c. Moreover, we confirm that this tentative trend is not due to inaccuracy in the period reported by J. M. Almenara et al. (2022). We repeat the fit described in Section 3.1 but setting a Gaussian prior on the orbital period centered on the value from J. M. Almenara et al. (2022) and with a width of 10 minutes in order to check whether the period inferred from these four transits disagreed with that published by J. M. Almenara et al. (2022). However, we find a period in perfect agreement with J. M. Almenara et al. (2022). A more complete fit including the transit and RV data from J. M. Almenara et al. (2022) may be able to provide better constraints on the eccentricity.

Appendix B Investigation into Stellar Activity Modeling

To make sure our retrieved shape in the transmission spectrum is independent of the activity event captured in our transit light curves, we explore fitting the flare using an asymmetric modified Lorentzian, an option within *Eureka!*’s Stage 5 to account for stellar variability. The Lorentzian model $L(t)$ as a function of time t is defined as

$$L(t) = 1 + \frac{A}{1 + x^p}, \quad (\text{B1})$$

such that $x = 2(t - t_0)/\text{WHM}$, where A is the amplitude, p is the exponent (where $p = 2$ for a standard Lorentzian), and WHM is the half-width at half-maximum. To create an asymmetric model representative of a flare, *Eureka!* allows for two independent Lorentzian models to fit the baseline before and after the flare midpoint t_0 . Therefore, we fit for two amplitudes, two HWHMs, one exponent, and one flare midpoint at the white light-curve stage for both NRS1 and NRS2. We only fit the spectroscopic light curves for the two amplitudes before and after midflare, while we fix the other Lorentzian parameters assuming that the shape of the flare is consistent across wavelengths.

Figure B1 shows the white light curve of GJ 3090 b’s transit for NRS1 and NRS2 and the described stellar model. It does reasonably well in capturing the flare’s shape; however, the residuals show that most data points lie below the model from just before the flare onward. We investigated whether this step in the data could be caused by a mirror tilt event as has been previously seen in other JWST data sets (e.g., L. Alderson et al. 2023). We did not find any evidence for a tilt event occurring in our observations as we did not observe a change in the position or width of the trace. In addition, the guide star data also did not show any significant jumps during our observations (as verified using the python tool *spelunker*; D. Deal & N. Espinoza 2024).

The retrieved transmission spectrum for visit 2 does not show any significant differences compared to the spectrum where the flare is not fitted; however, the uncertainties are larger in the case where the flare is removed and a GP captures any leftover stellar variations. We conclude that the best fit to the light curves is achieved by the GP as it results in less residual noise, and we argue that the larger uncertainties are more representative of the actual noise due to stellar variability in visit 2. Therefore, moving forward, we use the transmission spectrum where the stellar variability in the light curves is modeled by the GP and the flare is removed.

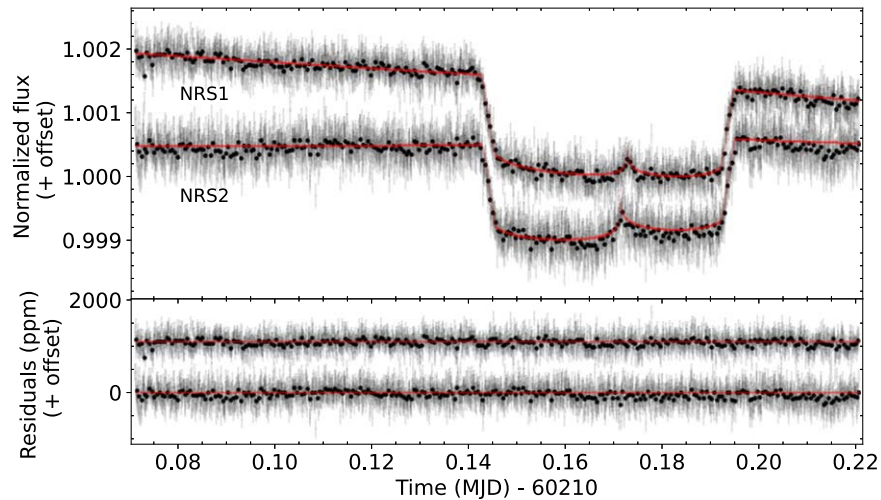


Figure B1. Visit 2: broadband (white) light curve of the transit of GJ 3090 b with a stellar flare (gray), using NIRSpc’s NRS1 and NRS2 detectors and the `Eureka!` pipeline. The black data points correspond to the flux binned (10 points) to aid visualization. The fits to both light curves are shown in red and include a transit model, a linear model, and a modified, asymmetric Lorentzian model to fit the flare. The residuals of the fits are shown in the bottom panel, displaying an offset in the data and the model after the flare.

Appendix C Stellar Heterogeneity Modeling

C.1. Modeling the NIRISS Out-of-transit Stellar Spectrum

In order to verify that the stellar surface heterogeneities that we retrieve from our TLS analysis are robust, we also directly model the out-of-transit stellar spectrum from each NIRISS/SOSS visit (e.g., H. R. Wakeford et al. 2019; S. E. Moran et al. 2023), closely following the methodology of M. Radica et al. (2025). We first flux-calibrate the extracted wavelength-dependent stellar spectra from each visit following the methods of O. Lim et al. (2023). We then median-combine the spectra along the temporal axis considering only the out-of-transit integrations, that is, integrations 1–350 and 660–779 for both visits. Like S. E. Moran et al. (2023), we use the standard deviation of the flux in each wavelength bin as the flux uncertainty.

We then fit one-, two-, and three-component stellar models to the data from each visit using the `StellarFit`²⁷ package (M. Radica et al. 2025). A one-component fit consists of a single PHOENIX stellar model (T.-O. Husser et al. 2013), with a given effective temperature and surface gravity, to represent a homogeneous stellar photosphere. Two- or three-component fits also include spots or spots and faculae, respectively, to model surface heterogeneities. A heterogeneous model is constructed using a weighted linear combination of a photosphere as well as spots and/or faculae, where each component is weighted by their covering fraction, and the photosphere is required to compose $>50\%$ of the stellar surface. All models are also scaled by R_*^2/D^2 using values from J. M. Almenara et al. (2022) for the stellar radius ($R_* = 0.516 R_\odot$) and the distance of the system to the Earth ($D = 22.45$ pc).

Unlike previous works, we do not consider only the best-fitting stellar model but fully sample the posterior space in order to obtain distributions on the acceptable ranges of heterogeneity parameters, analogous to our in-transit analysis. Moreover, as we use nested sampling, implemented via

`dynesty` (J. S. Speagle 2020), for the posterior exploration, we can also robustly ascertain whether heterogeneous models are truly statistically preferred over a homogeneous photosphere model instead of relying on the χ^2 statistic.

One-component fits have four free parameters: the stellar effective temperature, T_{phot} ; the surface gravity; a spectrum scaling factor; and a multiplicative error inflation term. The photosphere temperature was allowed to vary from 2300 to 5000 K, the gravity from 3.5 to 5, and the scale factor from 0.8 to 1.2. Multicomponent fits also include the spot/faculae temperature ($T_{\text{spot}}/T_{\text{fac}}$), covering fraction ($f_{\text{spot}}/f_{\text{fac}}$), and gravity. Spot/faculae temperatures are required to be at least 100 K and up to 1000 K cooler/warmer than the photosphere, whereas their gravity must be within 1.0 of the photosphere value. The best-fitting three-component results are shown in Figure C1.

In general, our out-of-transit spectrum analysis is consistent with the in-transit heterogeneity parameters. Visit 2 prefers (at $>3\sigma$ confidence) the presence of both spots and faculae over a homogeneous photosphere or spots/faculae alone. Like the in-transit analysis, we find the second visit to be dominated by spots, with minimal contributions from faculae. For visit 1, however, there is no strong statistical evidence for a heterogeneous photosphere—homogeneous and heterogeneous models fit the data equally well. This finding is slightly discrepant from the in-transit analysis, which weakly prefers the inclusion of spots; however, the retrieved spot parameters from the out-of-transit stellar spectrum are still broadly consistent with the in-transit findings.

It is also important to note that none of the stellar models are particularly good fits to the data, with χ_ν^2 values generally >150 . As shown in Figure C1, particularly at optical wavelengths, the models are poor representations of the observed spectra. With this in mind, although both the out-of- and in-transit analyses rely on stellar models, since the in-transit analysis uses *ratios* of models instead of *absolute fits*, it may be more robust against absolute inaccuracies in stellar models.

²⁷ <https://github.com/radicamc/StellarFit>

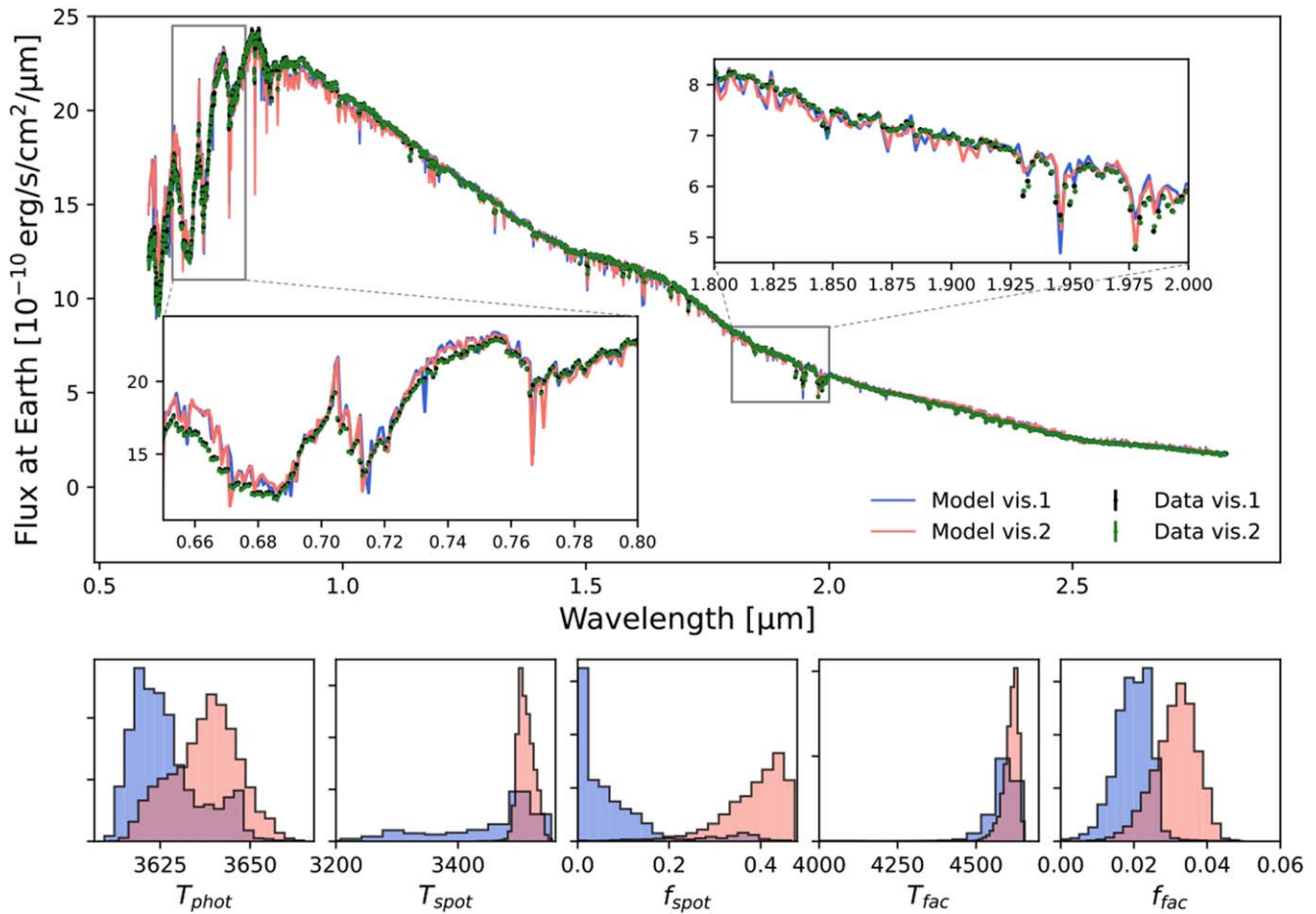


Figure C1. Constraints on stellar surface heterogeneities for both NIRISS/SOSS visits from the out-of-transit stellar spectra. Top: flux-calibrated NIRISS/SOSS stellar spectra using only the out-of-transit integrations (visit 1, black; visit 2, green) and best-fitting three-component PHOENIX model spectra (visit 1, blue; visit 2, red). Two $\sim 0.2 \mu\text{m}$ wavelength ranges are shown zoomed in in the insets to better visualize the higher-resolution structures. Bottom: retrieved photosphere temperature, as well as spot and faculae temperatures and covering fractions. Posteriors for visit 1 are shown in blue and visit 2 in red. The out-of-transit results are broadly consistent with the in-transit analysis in Section 6.1.

C.2. *stctm* TLS-only Modeling of the NIRISS Spectra

Stellar contamination can mimic atmospheric signatures in exoplanet transmission spectra, especially if they orbit M-type host stars (B. V. Rackham et al. 2018). Specifically, the presence of unocculted patches of the stellar surface that are colder than the photosphere (spots) can introduce spurious water absorption features and slopes of increasing transit depth toward the bluest wavelengths (A. R. Iyer & M. R. Line 2020; B. V. Rackham et al. 2023). The complex superposition of multiple heterogeneity temperatures and covering fractions can partially erase or even reverse such slopes while still altering the depth of any measured planetary absorption features and impacting the retrieved atmospheric properties. Our detection of a strong slope at short wavelengths in the spectra extracted from both NIRISS/SOSS visits motivates us to explore the impact of stellar contamination on our observations of GJ 3090 b.

The *stctm*²⁸ (C. Piaulet-Ghorayeb 2024) module performs forward modeling of stellar contamination spectra and retrievals of stellar heterogeneity properties from observations. The retrievals are run assuming the spectrum can be fully explained by unocculted faculae or spots on the stellar surface.

We model the planetary atmosphere’s contribution to the transmission spectrum as a wavelength-independent constant, D , and later perform joint retrievals including wavelength-dependent atmospheric signatures as well as stellar heterogeneities (Section 5.2.1).

The short-wavelength differences between the two NIRISS/SOSS spectra (Figure 3) suggest important visit-to-visit variations in the TLS signature (Figure 7). Meanwhile, the two NIRSpec visits preceded the first NIRISS visit by more than 2 months—significantly longer than the rotation period of the star. Combined with the ~ 100 ppm offset between the NIRISS and NIRSpec spectra, this prompts us to believe that the background stellar spot and faculae distributions were different during the NIRSpec observations than that observed at the epochs of the NIRISS observations. Since the NIRSpec spectra lack the critical short-wavelength coverage necessary to constrain independent TLS parameters from the NIRISS spectra (e.g., E. M. May et al. 2023; S. E. Moran et al. 2023), we choose to ignore the NIRSpec/G395H observations in our spot-only retrievals.

We perform a first set of retrievals assuming a single heterogeneity population consisting of stellar spots cooler than the photosphere. We applied these retrievals to both NIRISS/SOSS visits individually to determine whether they can be well described by stellar contamination alone and to search for

²⁸ <https://github.com/cpiaulet/stctm>

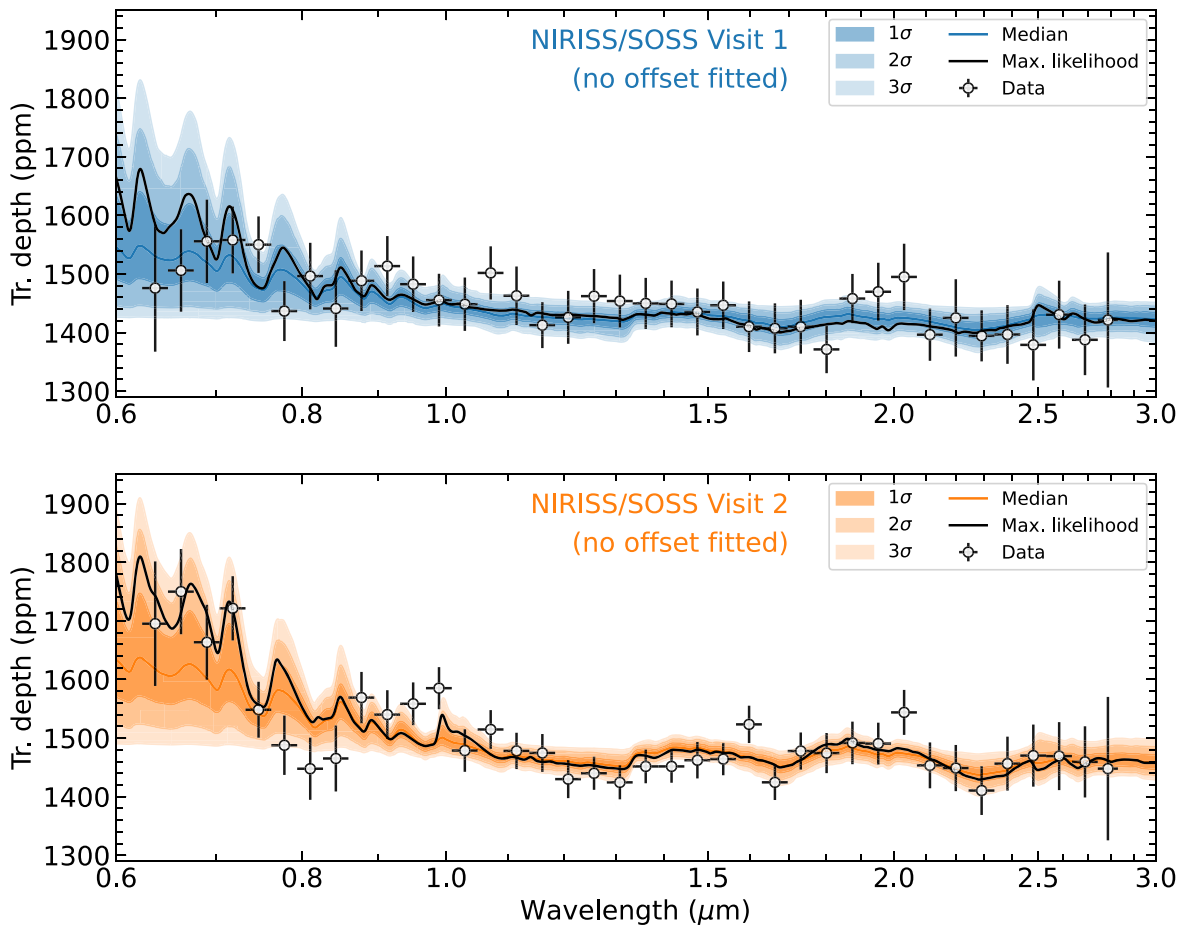


Figure C2. Results from the TLS-only fits to the transmission spectrum of each NIRISS/SOSS visit of GJ 3090 b from the `stctm` retrievals. We show the best-fitting unocculted heterogeneity model (black), as well as the median and 1σ , 2σ , and 3σ ranges obtained from sample posterior spectra (color shading). The top panel showcases the results for the fit to the visit 1 spectrum, and the bottom panel is the same result for the visit 2 spectrum. We show the binned (four points together) points for each visit (black points), with no offset applied between order 1 and order 2. The NIRISS/SOSS spectrum of GJ 3090 b is well matched by stellar contamination alone, in line with the lack of information content on the atmosphere we obtain from joint TLS–atmosphere retrievals over this wavelength range.

potential visit-to-visit variations in the heterogeneity makeup of the stellar surface.

We closely follow the steps outlined in C. Piaulet-Ghorayeb et al. (2024) and M. Radica et al. (2025) for the application of `stctm` to the TLS-only retrievals. The fitted parameters are the temperature differences between the heterogeneities and the photosphere: ΔT_{spot} , the photosphere temperature itself (T_{phot}), and the covering fraction of spots (f_{spot}). We calculate the spectra of each component by interpolating in the T_{eff} and $\log g$ dimensions over the PHOENIX stellar models grid (T.-O. Husser et al. 2013) using the `MSG` module (R. Townsend & A. Lopez 2023). Our priors are uniform between 0% and 50% for the heterogeneity covering fraction, uniform from -100 to -1000 K for the heterogeneity temperature contrast with the photosphere, and Gaussian for the photosphere temperature, with the mean and standard deviation informed by J. M. Almenara et al. (2022). We also use the newly introduced

(C. Piaulet-Ghorayeb et al. 2025, in preparation) fitting of the stellar photosphere $\log g$ ($\log g \in [2.5, 5.5]$) and of a potential difference between the surface gravities representative of the spectrum of the photosphere and stellar spot component (enforcing a $\log g$ for the spots equal to or lower than that of the photosphere; see, e.g., M. Fournier-Tondreau et al. 2024). We sample the parameter space using the `emcee` implementation of Markov Chain Monte Carlo (D. Foreman-Mackey et al. 2013), with 20 times as many walkers as fitted parameters. Each chain is run for 5000 steps and visually checked for convergence, and the first 60% of each chain is discarded as burn-in to obtain the distribution of posterior samples (results in Figures C2, C3, and 7). When the photosphere $\log g$ is fitted, we obtain consistent results in terms of the stellar heterogeneity properties for each visit, and the preferred value for the surface gravity is larger than the literature value.

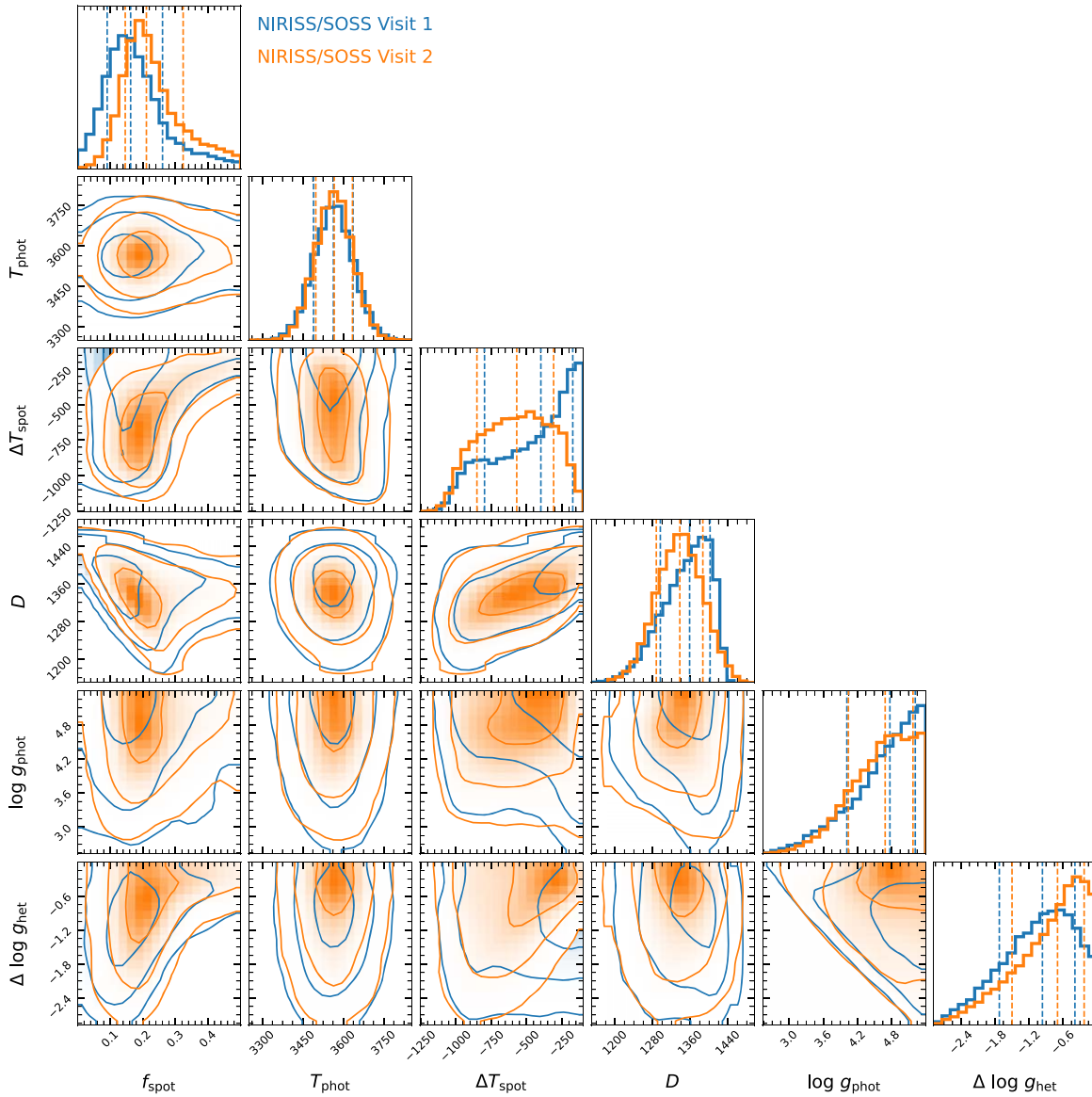


Figure C3. Joint and marginalized posterior distributions from the TLS-only fits to the transmission spectrum of each NIRISS/SOSS visit of GJ 3090 b performed using *stctm*. The contours correspond to 1σ , 2σ , and 3σ limits, and the median and 1σ interval are highlighted on each marginalized posterior distribution. The results for visit 1 (2) are shown in blue (orange).

Appendix D Atmosphere Retrieval Results

We report the constraints on atmospheric parameters from the atmosphere + TLS retrievals performed on the NIRISS/SOSS spectra in Table 5, which are mostly unconstrained since the spectrum can be fully explained by stellar contamination

alone. We also present a comparison between the posterior distributions on major absorbers obtained with the three retrieval frameworks from the retrievals performed on the NIRSpc/G395H transmission spectrum in Figure D1. The corresponding best-fit models for each retrieval code are shown in Figure D2.

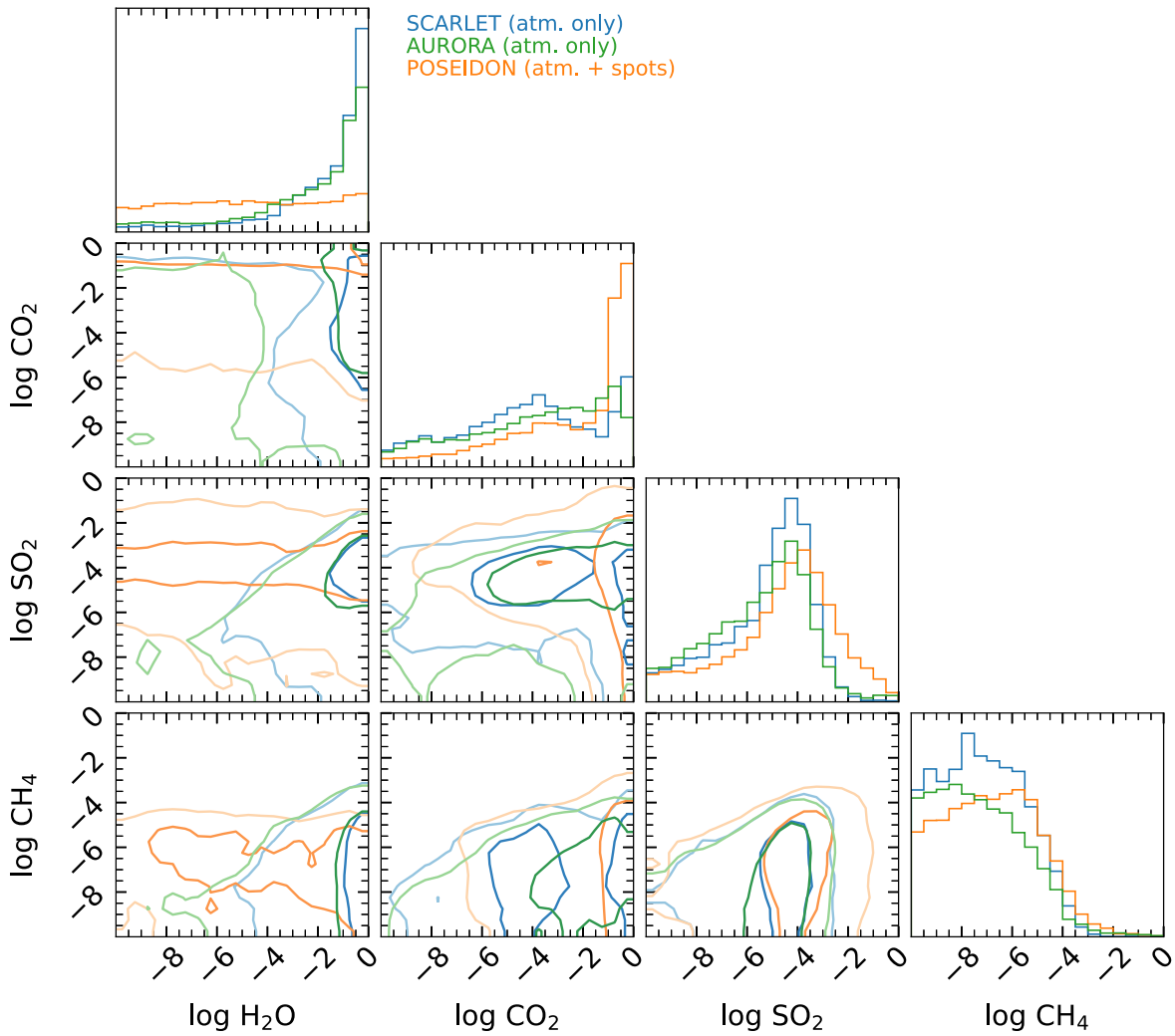


Figure D1. Joint and marginalized posterior distributions for the main atmospheric absorbers that NIRSpect/G395H is sensitive to from the SCARLET (blue), POSEIDON (orange), and AURORA (green) retrievals performed on the visit 1+2 NIRSpect/G395H spectrum of GJ 3090 b. While POSEIDON marginalized over the potential contributions from unocculted spots, the SCARLET and AURORA results shown do not account for a TLS contribution, leading to overall higher water abundances. The contours correspond to 1σ and 2σ confidence (dark and light shading).

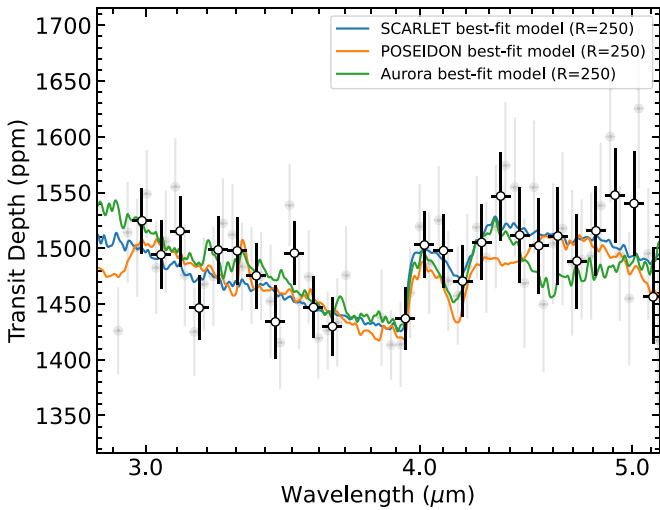


Figure D2. Best-fit models from the SCARLET (blue), POSEIDON (orange), and Aurora (green) retrievals performed on the NIRSpect/G395H transmission spectrum of GJ 3090 b (gray points at $R=100$, binned in black), corresponding to the posterior plot shown in Figure D1. The three models were smoothed to a resolving power of 250.

Appendix E Additional Figures

Figure E1 shows the NIRSpect/G395H white light curves for NRS2 without any integrations cut as a result of systematics or flares.

In Figure E2, the second independent reductions for both NIRSpect and NIRISS are displayed. The left panels show the spectrum of the NIRSpect data retrieved using Eureka!, with the top panel comparing the two visits with each other and the bottom panel displaying the comparison between our nominal exoTDRF reduction. Similarly, for NIRISS/SOSS, we show the two visits of our second independent analysis using the NAMELESS pipeline for the data reduction and the Tiberius pipeline for light-curve fitting in the right panels of Figure E2. In the top panel, we show both visits of the NAMELESS reduction, while the bottom panel compares both visits and both reductions directly, demonstrating that the GPs used in the light-curve fitting in the exoTDRF reduction significantly increase the uncertainties for the transmission spectrum. Nevertheless, both reductions show differences between the two visits that are consistent and

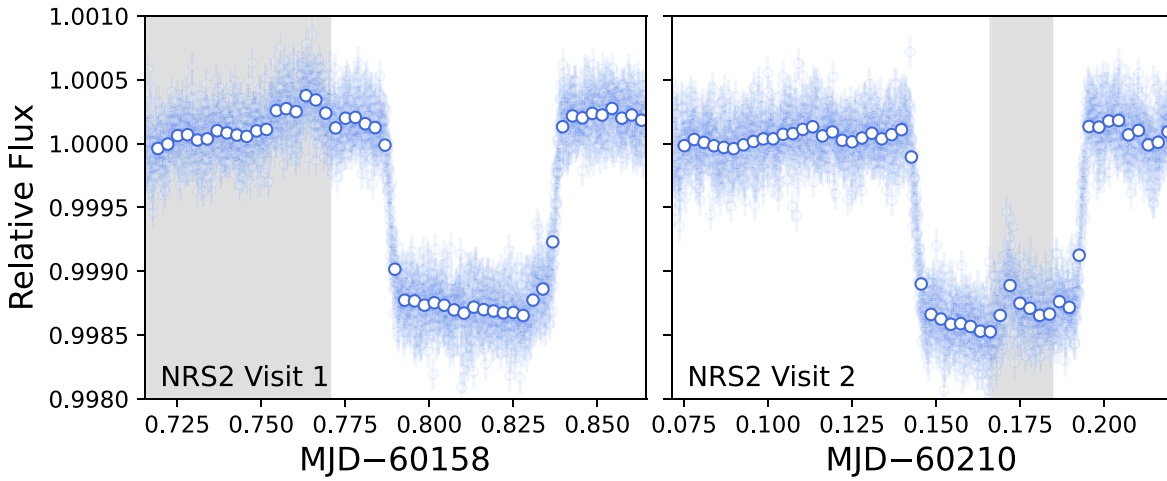


Figure E1. Raw NRS2 white light curves for each NIRSpec/G395H without any integrations cut as a result of systematics (visit 1) or flares (visit 2). The gray shaded regions denote the integrations that are cut in the light-curve analysis presented in Section 3.1.

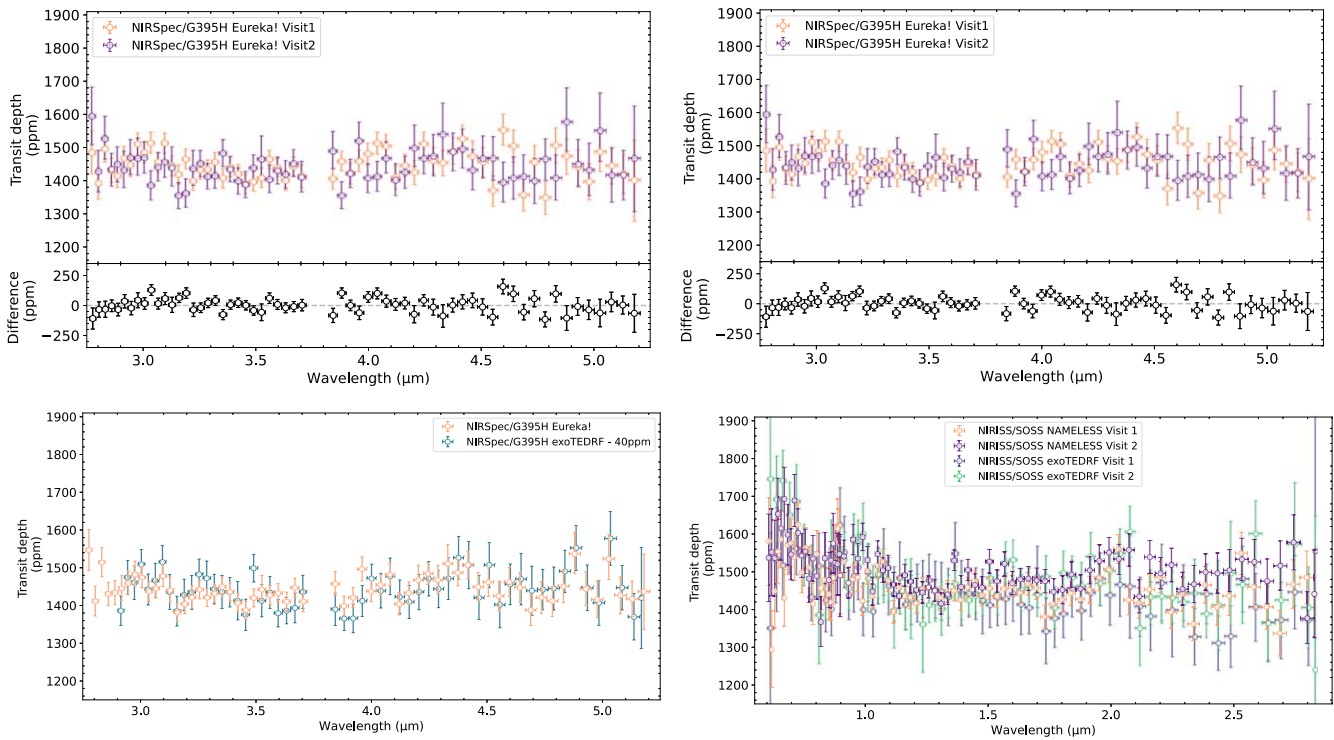


Figure E2. Comparison of transmission spectra of GJ 3090 b from different reduction pipelines. Top left: Eureka! transmission spectra from both NIRSpec/G395H visits. Visit 1 is displayed in the darker purple color and visit 2 in the lighter orange color, and the differences between them are shown in the bottom panel in black. Bottom left: combined (visit 1 and visit 2) NIRSpec transmission spectra from Eureka! (orange) and exoTDRF (turquoise). The latter reduction is vertically offset by their average difference of 40 ppm to allow for direct comparison. Top right: NAMELESS transmission spectra of GJ 3090 b from both NIRISS/SOSS visits. Visit 1 is displayed in orange and visit 2 in purple. The differences between the two visits are shown in the bottom panel in black, demonstrating a ~ 30 ppm offset between the two visits. Bottom right: comparison of the NAMELESS (orange, purple) and exoTDRF (turquoise, dark blue) transmission spectra for both NIRISS/SOSS visits.

showcase that the NIRISS/SOSS observations cannot be combined if the stellar activity level has changed in the time passed between the two visits.

Lastly, we show in Figure E3 the range of grid model spectra and parameters that match the NIRSpec/G395H spectrum of GJ 3090 b.

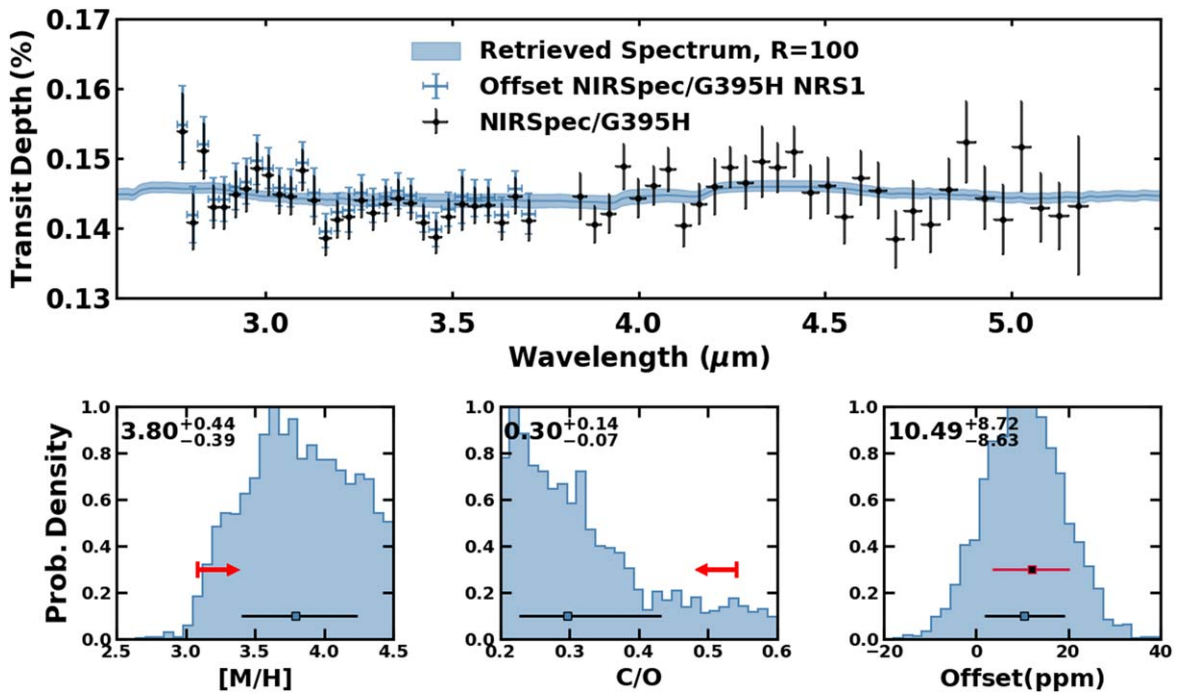


Figure E3. Top: the retrieved spectrum from the grid-based 1D-RCTE retrieval with `SCCHIMERA`. Shaded is the 1σ confidence region about the median model, plotted as a solid line. The blue points are the NRS1 points with the median retrieved instrument offset of 10.49 ppm. Bottom panels: the posterior probability density distributions for [M/H], where [] denotes \log_{10} relative to solar, C/O, and the instrument offset on NIRSspec/G395H NRS1. Points with error bars denote the median and 1σ confidence region on each parameter. The red points show parameter constraints from the disequilibrium retrieval. Arrows mark the 2σ lower limit for M/H and the 1σ preference for C/O.

ORCID iDs

Eva-Maria Ahrer <https://orcid.org/0000-0003-0973-8426>
 Michael Radica <https://orcid.org/0000-0002-3328-1203>
 Caroline Piaulet-Ghorayeb <https://orcid.org/0000-0002-2875-917X>
 Eshan Raul <https://orcid.org/0009-0002-2380-6683>
 Lindsey Wisner <https://orcid.org/0000-0002-3295-1279>
 Luis Welbanks <https://orcid.org/0000-0003-0156-4564>
 Lorena Acuña <https://orcid.org/0000-0002-9147-7925>
 Romain Allart <https://orcid.org/0000-0002-1199-9759>
 Louis-Philippe Coulombe <https://orcid.org/0000-0002-2195-735X>
 Amy Louca <https://orcid.org/0000-0002-3191-2200>
 Ryan MacDonald <https://orcid.org/0000-0003-4816-3469>
 Morgan Saidel <https://orcid.org/0000-0001-9518-9691>
 Thomas M. Evans-Soma <https://orcid.org/0000-0001-5442-1300>
 Björn Benneke <https://orcid.org/0000-0001-5578-1498>
 Duncan Christie <https://orcid.org/0000-0002-4997-0847>
 Thomas G. Beatty <https://orcid.org/0000-0002-9539-4203>
 Charles Cadieux <https://orcid.org/0000-0001-9291-5555>
 Ryan Cloutier <https://orcid.org/0000-0001-5383-9393>
 René Doyon <https://orcid.org/0000-0001-5485-4675>
 Jonathan J. Fortney <https://orcid.org/0000-0002-9843-4354>
 Anna Gagnebin <https://orcid.org/0009-0003-2576-9422>
 Cyril Gapp <https://orcid.org/0009-0007-9356-8576>
 Hamish Innes <https://orcid.org/0000-0001-5271-0635>
 Heather A. Knutson <https://orcid.org/0000-0002-5375-4725>
 Thaddeus Komacek <https://orcid.org/0000-0002-9258-5311>
 Joshua Krissansen-Totton <https://orcid.org/0000-0001-6878-4866>
 Yamila Miguel <https://orcid.org/0000-0002-0747-8862>

Raymond Pierrehumbert <https://orcid.org/0000-0002-5887-1197>

Pierre-Alexis Roy <https://orcid.org/0000-0001-6809-3520>

Hilke E. Schlichting <https://orcid.org/0000-0002-0298-8089>

References

- Acuna, L., Deleuil, M., & Mousis, O. 2023, *A&A*, 677, A14
 Acuña, L., Deleuil, M., Mousis, O., et al. 2021, *A&A*, 647, A53
 Acuña, L., Kreidberg, L., Zhai, M., & Mollière, P. 2024, *A&A*, 688, A60
 Aguichine, A., Mousis, O., Deleuil, M., & Marcq, E. 2021, *ApJ*, 914, 84
 Aguichine, A., Mousis, O., Devouard, B., & Ronnet, T. 2020, *ApJ*, 901, 97
 Ahrer, E., Wheatley, P. J., Kirk, J., et al. 2022, *MNRAS*, 510, 4857
 Ahrer, E. M., Stevenson, K. B., Mansfield, M., et al. 2023, *Natur*, 614, 653
 Albert, L., Lafrenière, D., Renè, D., et al. 2023, *PASP*, 135, 075001
 Alderson, L., Batalha, N. E., Wakeford, H. R., et al. 2024, *AJ*, 167, 216
 Alderson, L., Wakeford, H. R., Alam, M. K., et al. 2023, *Natur*, 614, 664
 Alibert, Y., & Benz, W. 2017, *A&A*, 598, L5
 Allart, R., Bourrier, V., Lovis, C., et al. 2019, *A&A*, 623, A58
 Almenara, J. M., Bonfils, X., Otegi, J. F., et al. 2022, *A&A*, 665, A91
 Asplund, M., Grevesse, N., Sauval, A. J., & Scott, P. 2009, *ARA&A*, 47, 481
 Astropy Collaboration, Price-Whelan, A. M., Sipőcz, B. M., et al. 2018, *AJ*, 156, 123
 Astropy Collaboration, Robitaille, T. P., Tollerud, E. J., et al. 2013, *A&A*, 558, A33
 Azzam, A. A. A., Yurchenko, S. N., Tennyson, J., & Naumenko, O. V. 2016, *MNRAS*, 460, 4063
 Banerjee, A., Barstow, J. K., Gressier, A., et al. 2024, *ApJL*, 975, L11
 Barclay, T., Kostov, V. B., Colón, K. D., et al. 2021, *AJ*, 162, 300
 Bean, J. L., Désert, J.-M., Seifahrt, A., et al. 2013, *ApJ*, 771, 108
 Beatty, T. G., Welbanks, L., Schlawin, E., et al. 2024, *ApJL*, 970, L10
 Bell, T. J., Ahrer, E.-M., Brande, J., et al. 2022, *JOSS*, 7, 4503
 Benneke, B. 2015, arXiv:1504.07655
 Benneke, B., Knutson, H. A., Lothringer, J., et al. 2019a, *NatAs*, 3, 813
 Benneke, B., Roy, P.-A., Coulombe, L.-P., et al. 2024, arXiv:2403.03325
 Benneke, B., & Seager, S. 2012, *ApJ*, 753, 100
 Benneke, B., & Seager, S. 2013, *ApJ*, 778, 153

- Benneke, B., Wong, I., Piaulet, C., et al. 2019b, *ApJL*, **887**, L14
- Berta, Z. K., Charbonneau, D., Désert, J.-M., et al. 2012, *ApJ*, **747**, 35
- Bézar, B., Charnay, B., & Blain, D. 2022, *NatAs*, **6**, 537
- Biassoni, F., Caldiroli, A., et al. 2024, *A&A*, **682**, A115
- Birkmann, S. M., Ferruit, P., Giardino, G., et al. 2022, *A&A*, **661**, A83
- Bitsch, B., Raymond, S. N., Buchhave, L. A., et al. 2021, *A&A*, **649**, L5
- Borucki, W. J., Koch, D., Basri, G., et al. 2010, *Sci*, **327**, 977
- Bouchy, F., Doyon, R., Artigau, É., et al. 2017, *Msngr*, **169**, 21
- Buchner, J., Georgakakis, A., Nandra, K., et al. 2014, *A&A*, **564**, A125
- Burn, R., Mordasini, C., Mishra, L., et al. 2024, *NatAs*, **8**, 463
- Bushouse, H., Eisenhamer, J., Dencheva, N., et al. 2023, JWST Calibration Pipeline, v1.11.3, Zenodo, doi:10.5281/zenodo.8157276
- Cadioux, C., Doyon, R., MacDonald, R. J., et al. 2024, *ApJL*, **970**, L2
- Caldirola, A., Haardt, F., et al. 2021, *A&A*, **655**, A30
- Chachan, Y., & Stevenson, D. J. 2018, *ApJ*, **854**, 21
- Charbonneau, D., Brown, T. M., Latham, D. W., & Mayor, M. 2000, *ApJ*, **529**, L45
- Cherubim, C., Wordsworth, R., Bower, D., et al. 2025, *ApJ*, **983**, 97
- Cherubim, C., Wordsworth, R., Hu, R., & Shkolnik, E. 2024, *ApJ*, **967**, 139
- Cloutier, R., & Menou, K. 2020, *AJ*, **159**, 211
- Coles, P. A., Yurchenko, S. N., & Tennyson, J. 2019, *MNRAS*, **490**, 4638
- Cooke, G. J., & Madhusudhan, N. 2024, *ApJ*, **977**, 209
- Coulombe, L.-P., Benneke, B., Challener, R., et al. 2023, *Natur*, **620**, 292
- Coulombe, L.-P., Radica, M., Benneke, B., et al. 2025, *NatAs*, **9**, 512
- Coulombe, L.-P., Roy, P.-A., & Benneke, B. 2024, *AJ*, **168**, 227
- Darveau-Bernier, A., Albert, L., Talens, G. J., et al. 2022, *PASP*, **134**, 094502
- Deal, D., & Espinoza, N. 2024, *JOSS*, **9**, 6202
- Dos Santos, L. A., Alam, M. K., Espinoza, N., & Vissapragada, S. 2023, *AJ*, **165**, 244
- Dos Santos, L. A., Vidotto, A. A., et al. 2022, *A&A*, **659**, A62
- Doyon, R., Willott, C. J., Hutchings, J. B., et al. 2023, *PASP*, **135**, 098001
- Edwards, B., Changeat, Q., Mori, M., et al. 2021, *AJ*, **161**, 44
- Ehrenreich, D., Bourrier, V., Wheatley, P., et al. 2015, *Natur*, **522**, 459
- Erkaev, N. V., Kulikov, Y. N., Lammer, H., et al. 2007, *A&A*, **472**, 329
- Feinstein, A. D., Radica, M., Welbanks, L., et al. 2023, *Natur*, **614**, 670
- Feroz, F., Hobson, M. P., & Bridges, M. 2009, *MNRAS*, **398**, 1601
- Foreman-Mackey, D., Agol, E., Ambikasaran, S., & Angus, R. 2017, *AJ*, **154**, 220
- Foreman-Mackey, D., Hogg, D. W., Lang, D., & Goodman, J. 2013, *PASP*, **125**, 306
- Fortney, J. J., Marley, M. S., & Barnes, J. W. 2007, *ApJ*, **659**, 1661
- Fortney, J. J., Mordasini, C., Nettelmann, N., et al. 2013, *ApJ*, **775**, 80
- Fortney, J. J., Visscher, C., Marley, M. S., et al. 2020, *AJ*, **160**, 288
- Fossati, L., Pillitteri, I., Shaikhislamov, I. F., et al. 2023, *A&A*, **673**, A37
- Fournier-Tondreau, M., MacDonald, R. J., Radica, M., et al. 2024, *MNRAS*, **528**, 3354
- Fu, G., Espinoza, N., Sing, D., et al. 2023, AAS Meeting, **241**, 159.04
- Fulton, B. J., & Petigura, E. A. 2018, *AJ*, **156**, 264
- Fulton, B. J., Petigura, E. A., Howard, A. W., et al. 2017, *AJ*, **154**, 109
- Gao, P., Piette, A. A. A., Steinrueck, M. E., et al. 2023, *ApJ*, **951**, 96
- Ginzburg, S., Schlichting, H. E., & Sari, R. 2016, *ApJ*, **825**, 29
- Ginzburg, S., Schlichting, H. E., & Sari, R. 2018, *MNRAS*, **476**, 759
- Glein, C. R. 2024, *ApJL*, **964**, L19
- Gordon, S., & McBride, B. J. 1994, Computer Program for Calculation of Complex Chemical Equilibrium Compositions and Applications. Part 1: Analysis Tech. Rep. 19950013764, NASA Lewis Research Center
- Grant, D., & Wakeford, H. 2024, *JOSS*, **9**, 6816
- Gressier, A., Espinoza, N., Allen, N. H., et al. 2024, *ApJL*, **975**, L10
- Grimm, S. L., & Heng, K. 2015, *ApJ*, **808**, 182
- Guilluy, G., D'Arpa, M. C., Bonomo, A. S., et al. 2024, *A&A*, **686**, A83
- Gupta, A., & Schlichting, H. E. 2019, *MNRAS*, **487**, 24
- Gupta, A., & Schlichting, H. E. 2020, *MNRAS*, **493**, 792
- Haldemann, J., Alibert, Y., Mordasini, C., & Benz, W. 2020, *A&A*, **643**, A105
- Handley, W. J., Hobson, M. P., & Lasenby, A. N. 2015a, *MNRAS*, **453**, 4384
- Handley, W. J., Hobson, M. P., & Lasenby, A. N. 2015b, *MNRAS: Letters*, **450**, L61
- Hargreaves, R. J., Gordon, I. E., Rey, M., et al. 2020, *ApJS*, **247**, 55
- Hargreaves, R. J., Gordon, I. E., Rothman, L. S., et al. 2019, *JQSRT*, **232**, 35
- Harris, C. R., Millman, K. J., van der Walt, S. J., et al. 2020, *Natur*, **585**, 357
- Harris, G. J., Tennyson, J., Kaminsky, B. M., Pavlenko, Y. V., & Jones, H. R. A. 2006, *MNRAS*, **367**, 400
- Helled, R., & Howard, S. 2024, arXiv:2407.05853
- Henry, G. W., Marcy, G. W., Butler, R. P., & Vogt, S. S. 2000, *ApJ*, **529**, L41
- Ho, C. S. K., Rogers, J. G., Van Eylen, V., Owen, J. E., & Schlichting, H. E. 2024, *MNRAS*, **531**, 3698
- Holmberg, M., & Madhusudhan, N. 2024, *A&A*, **683**, L2
- Howard, W. S., Kowalski, A. F., Flagg, L., et al. 2023, *ApJ*, **959**, 64
- Hunter, J. D. 2007, *CSE*, **9**, 90
- Husser, T.-O., Wende-von Berg, S., Dreizler, S., et al. 2013, *A&A*, **553**, A6
- Innes, H., Tsai, S.-M., & Pierrehumbert, R. T. 2023, *ApJ*, **953**, 168
- Iyer, A. R., & Line, M. R. 2020, *ApJ*, **889**, 78
- Iyer, A. R., Line, M. R., Muirhead, P. S., Fortney, J. J., & Gharib-Nezhad, E. 2023, *ApJ*, **944**, 41
- Kempton, E. M. R., Zhang, M., Bean, J. L., et al. 2023, *Natur*, **620**, 67
- Kirk, J., Alam, M. K., Lopez-Morales, M., & Zeng, L. 2020, *AJ*, **159**, 115
- Kirk, J., Rackham, B. V., MacDonald, R. J., et al. 2021, *AJ*, **162**, 34
- Kirk, J., Wheatley, P. J., Loudon, T., et al. 2017, *MNRAS*, **468**, 3907
- Kite, E. S., Fegley, B., Jr., Schaefer, L., & Ford, E. B. 2019, *ApJL*, **887**, L33
- Kite, E. S., & Ford, E. B. 2018, *ApJ*, **864**, 75
- Kite, E. S., & Schaefer, L. 2021, *ApJL*, **909**, L22
- Kostogryz, N., Shapiro, A., Witzke, V., et al. 2023, *RNAAS*, **7**, 39
- Kreidberg, L. 2015, *PASP*, **127**, 1161
- Kreidberg, L., Bean, J. L., Désert, J.-M., et al. 2014, *Natur*, **505**, 69
- Lammer, H., Selsis, F., Ribas, I., et al. 2003, *ApJL*, **598**, L121
- Leconte, J., Spiga, A., Clément, N., et al. 2024, *A&A*, **686**, A131
- Lee, E. J., & Chiang, E. 2016, *ApJ*, **817**, 90
- Lichtenberg, T., Bower, D. J., Hammond, M., et al. 2021, *JGRE*, **126**, e2020JE006711
- Lichtenberg, T., & Miguel, Y. 2025, *TrGeo*, **7**, 51
- Lim, O., Benneke, B., Doyon, R., et al. 2023, *ApJL*, **955**, L22
- Line, M. R., & Parmentier, V. 2016, *ApJ*, **820**, 78
- Lopez, E. D., & Fortney, J. J. 2014, *ApJ*, **792**, 1
- Lopez, E. D., Fortney, J. J., & Miller, N. 2012, *ApJ*, **761**, 59
- Lucy, L. B., & Sweeney, M. A. 1971, *AJ*, **76**, 544
- Luger, R., Barnes, R., Lopez, E., et al. 2015, *AsBio*, **15**, 57
- Luo, H., Dorn, C., & Deng, J. 2024, *NatAs*, **8**, 1399
- Luque, R., & Pallé, E. 2022, *Sci*, **377**, 1211
- Léger, A., Selsis, F., Sotin, C., et al. 2004, *Icar*, **169**, 499
- MacDonald, R. J. 2023, *JOSS*, **8**, 4873
- MacDonald, R. J., & Lewis, N. K. 2022, *ApJ*, **929**, 20
- MacDonald, R. J., & Madhusudhan, N. 2017, *MNRAS*, **469**, 1979
- Madhusudhan, N., Piette, A. A. A., & Constantinou, S. 2021, *ApJ*, **918**, 1
- Madhusudhan, N., Sarkar, S., Constantinou, S., et al. 2023, *ApJL*, **956**, L13
- Madhusudhan, N., & Seager, S. 2009, *ApJ*, **707**, 24
- Mah, J., Savvidou, S., & Bitsch, B. 2024, *A&A*, **686**, L17
- Malsky, I., Rogers, L., Kempton, E. M. R., & Marounina, N. 2022, *NatAs*, **7**, 57
- Mansfield, M., Bean, J. L., Oklopčić, A., et al. 2018, *ApJL*, **868**, L34
- Mansfield, M., Line, M. R., Bean, J. L., et al. 2021, *NatAs*, **5**, 1224
- May, E. M., MacDonald, R. J., Bennett, K. A., et al. 2023, *ApJL*, **959**, L9
- Mayor, M., Pepe, F., Queloz, D., et al. 2003, *Msngr*, **114**, 20
- Mayor, M., & Queloz, D. 1995, *Natur*, **378**, 355
- Mikal-Evans, T., Madhusudhan, N., Dittmann, J., et al. 2023, *AJ*, **165**, 84
- Mollière, P., van Boekel, R., Dullemond, C., Henning, T., Mordasini, C., et al. 2015, *ApJ*, **813**, 47
- Moran, S. E., Stevenson, K. B., Sing, D. K., et al. 2023, *ApJL*, **948**, L11
- Mousis, O., Deleuil, M., Aguichine, A., et al. 2020, *ApJL*, **896**, L22
- Mousis, O., Ronnet, T., & Lunine, J. I. 2019, *ApJ*, **875**, 9
- Northmann, L., Pallé, E., Salz, M., et al. 2018, *Sci*, **362**, 1388
- Ohno, K., Schlawin, E., Bell, T. J., et al. 2025, *ApJL*, **979**, L7
- Oklopčić, A. 2019, *ApJ*, **881**, 133
- Oklopčić, A., & Hirata, C. M. 2018, *ApJL*, **855**, L11
- Orell-Miquel, J., Murgas, F., Pallé, E., et al. 2024, *A&A*, **689**, A179
- Otegi, J. F., Dorn, C., Helled, R., et al. 2020, *A&A*, **640**, A135
- Owen, J. E., & Jackson, A. P. 2012, *MNRAS*, **425**, 2931
- Owen, J. E., & Murray-Clay, R. 2018, *MNRAS*, **480**, 2206
- Owen, J. E., & Wu, Y. 2017, *ApJ*, **847**, 29
- Parker, L. T., Mendonça, J. M., Diamond-Lowe, H., et al. 2025, *MNRAS*, **538**, 3263
- Pelletier, S., Benneke, B., Darveau-Bernier, A., et al. 2021, *AJ*, **162**, 73
- Pérez, F., & Granger, B. E. 2007, *CSE*, **9**, 21
- Petigura, E. A., Rogers, J. G., Isaacson, H., et al. 2022, *AJ*, **163**, 179
- Piaulet, C., Benneke, B., Almenara, J. M., et al. 2023, *NatAs*, **7**, 206
- Piaulet-Ghorayeb, C. 2024, First Release of Stellar Contamination Modeling and Retrieval Code, v1.0.0, Zenodo, doi:10.5281/zenodo.13153252
- Piaulet-Ghorayeb, C., Benneke, B., Radica, M., et al. 2024, *ApJL*, **974**, L10
- Pinhas, A., Rackham, B. V., Madhusudhan, N., & Apai, D. 2018, *MNRAS*, **480**, 5314
- Polyansky, O. L., Kyuberis, A. A., Zobov, N. F., et al. 2018, *MNRAS*, **480**, 2597
- Rackham, B. V., Apai, D., & Giampapa, M. S. 2018, *ApJ*, **853**, 122
- Rackham, B. V., Apai, D., & Giampapa, M. S. 2019, *AJ*, **157**, 96

- Rackham, B. V., Espinoza, N., Berdyugina, S. V., et al. 2023, *RASTI*, **2**, 148
- Radica, M. 2024a, *JOSS*, **9**, 6898
- Radica, M. 2024b, *radicamc/exoUPRF*: v1.0.1, Zenodo, doi:10.5281/zenodo.12628066
- Radica, M., Albert, L., Taylor, J., et al. 2022, *PASP*, **134**, 104502
- Radica, M., Coulombe, L.-P., Taylor, J., et al. 2024, *ApJL*, **962**, L20
- Radica, M., Piaulet-Ghorayeb, C., Taylor, J., et al. 2025, *ApJL*, **979**, L5
- Radica, M., Welbanks, L., Espinoza, N., et al. 2023, *MNRAS*, **524**, 835
- Ricker, G. R., Winn, J. N., Vanderspek, R., et al. 2015, *JATIS*, **1**, 014003
- Rigby, F. E., Pica-Ciamarra, L., Holmberg, M., et al. 2024, *ApJ*, **975**, 101
- Rogers, J. G., Gupta, A., Owen, J. E., & Schlichting, H. E. 2021, *MNRAS*, **508**, 5886
- Rogers, J. G., Schlichting, H. E., & Owen, J. E. 2023, *ApJL*, **947**, L19
- Rogers, J. G., Schlichting, H. E., & Young, E. D. 2024, *ApJ*, **970**, 47
- Rogers, L. A., & Seager, S. 2010, *ApJ*, **712**, 974
- Roy, P.-A., Benneke, B., Piaulet, C., et al. 2023, *ApJL*, **954**, L52
- Salz, M., Czesla, S., Schneider, P. C., & Schmitt, J. H. M. M. 2016, *A&A*, **586**, A75
- Schlawin, E., Ohno, K., Bell, T. J., et al. 2024, *ApJL*, **974**, L33
- Schlichting, H. E., & Young, E. D. 2022, *PSJ*, **3**, 127
- Schmidt, S. P., MacDonald, R. J., Tsai, S.-M., et al. 2025, arXiv:2501.18477
- Seager, S., & Mallén-Ornelas, G. 2003, *ApJ*, **585**, 1038
- Shuttle, O., Jordan, S., Nicholls, H., Lichtenberg, T., & Bower, D. J. 2024, *ApJL*, **962**, L8
- Skilling, J. 2004, *AIPC*, **735**, 395
- Skilling, J. 2006, *BayAn*, **1**, 833
- Skrutskie, M. F., Cutri, R. M., Stiening, R., et al. 2006, *AJ*, **131**, 1163
- Spake, J. J., Oklopčic, A., & Hillenbrand, L. A. 2021, *AJ*, **162**, 284
- Spake, J. J., Sing, D. K., Evans, T. M., et al. 2018, *Natur*, **557**, 68
- Speagle, J. S. 2020, *MNRAS*, **493**, 3132
- Teske, J., Batalha, N. E., Wallack, N. L., et al. 2025, *AJ*, **169**, 249
- Townsend, R., & Lopez, A. 2023, *JOSS*, **8**, 4602
- Trotta, R. 2008, *ConPh*, **49**, 71
- Tsai, S. M., Lee, E. K., Powell, D., et al. 2023, *Natur*, **617**, 483
- Tsai, S.-M., Lee, E. K. H., & Pierrehumbert, R. 2022, *A&A*, **664**, A82
- Tsai, S.-M., Lyons, J. R., Grosheintz, L., et al., 2017 VULCAN: Chemical Kinetics For Exoplanetary Atmospheres, Astrophysics Source Code Library, ascl:1704.011
- Tsiaras, A., Waldmann, I. P., Tinetti, G., Tennyson, J., & Yurchenko, S. N. 2019, *NatAs*, **3**, 1086
- Underwood, D. S., Tennyson, J., Yurchenko, S. N., et al. 2016, *MNRAS*, **459**, 3890
- Valencia, D. 2010, in IAU Symp. 276, The Astrophysics of Planetary Systems: Formation, Structure, and Dynamical Evolution, ed. A. Sozzetti, M. G. Lattanzi, & A. P. Boss (Cambridge, UK: Cambridge Univ. Press), 181
- Vazan, A., Sari, R., & Kessel, R. 2022, *ApJ*, **926**, 150
- Venturini, J., Guilera, O. M., Haldemann, J., Ronco, M. P., & Mordasini, C. 2020, *A&A*, **643**, L1
- Venturini, J., Ronco, M. P., Guilera, O. M., et al. 2024, *A&A*, **686**, L9
- Vidal-Madjar, A., Lecavelier des Etangs, A., Désert, J. M., et al. 2003, *Natur*, **422**, 143
- Virtanen, P., Gommers, R., Oliphant, T. E., et al. 2020, *NatMe*, **17**, 261
- Vissapragada, S., Greklek-McKeon, M., Linssen, D., et al. 2024a, *AJ*, **167**, 199
- Vissapragada, S., McCreery, P., Dos Santos, L. A., et al. 2024b, *ApJL*, **962**, L19
- von Zahn, U., & Hunten, D. M. 1996, *Sci*, **272**, 849
- von Zahn, U., Hunten, D. M., & Lehmacher, G. 1998, *JGR*, **103**, 22815
- Wakeford, H. R., Wilson, T. J., Stevenson, K. B., & Lewis, N. K. 2019, *RNAAS*, **3**, 7
- Wallack, N. L., Batalha, N. E., Alderson, L., et al. 2024, *AJ*, **168**, 77
- Watson, A. J., Donahue, T. M., & Walker, J. C. G. 1981, *Icar*, **48**, 150
- Welbanks, L., Bell, T. J., Beatty, T. G., et al. 2024, *Natur*, **630**, 836
- Welbanks, L., & Madhusudhan, N. 2019, *AJ*, **157**, 206
- Welbanks, L., & Madhusudhan, N. 2021, *ApJ*, **913**, 114
- Wogan, N. F., Batalha, N. E., Zahnle, K., et al. 2024, *ApJL*, **963**, L7
- Xue, Q., Bean, J. L., Zhang, M., et al. 2024, *ApJL*, **963**, L5
- Youngblood, A., France, K., Loyd, R. O. P., et al. 2016, *ApJ*, **824**, 101
- Yurchenko, S. N., Mellor, T. M., Freedman, R. S., & Tennyson, J. 2020, *MNRAS*, **496**, 5282
- Zamyatina, M., Christie, D. A., Hébrard, E., et al. 2024, *MNRAS*, **529**, 1776
- Zamyatina, M., Hébrard, E., Drummond, B., et al. 2023, *MNRAS*, **519**, 3129
- Zhang, M., Bean, J. L., Wilson, D., et al. 2025, *AJ*, **169**, 204
- Zhang, M., Knutson, H. A., Dai, F., et al. 2023, *AJ*, **165**, 62
- Zhang, M., Knutson, H. A., Wang, L., Dai, F., & Barragán, O. 2022a, *AJ*, **163**, 67
- Zhang, M., Knutson, H. A., Wang, L., et al. 2022b, *AJ*, **163**, 68
- Zieba, S., Kreidberg, L., Ducrot, E., et al. 2023, *Natur*, **620**, 746